Department of Materials Science and Engineering

Thermodynamic properties of selected phases in the MgO-Sb-O, CaO-Te-O, Pt-Te-O, and Al_2O_3-Cu-O systems by the EMF method

Dmitry Sukhomlinov

Aalto University

DOCTORAL DISSERTATIONS

Aalto University publication series
DOCTORAL DISSERTATIONS 5/2017

Thermodynamic properties of selected phases in the MgO-Sb-O, CaO-Te-O, Pt-Te-O, and Al_2O_3-Cu-O systems by the EMF method

Dmitry Sukhomlinov

A doctoral dissertation completed for the degree of Doctor of Science (Technology) to be defended, with the permission of the Aalto University School of Chemical Technology, at a public examination held at the lecture hall V1 of the school on 3 February 2017 at 12.

Aalto University
School of Chemical Technology
Department of Materials Science and Engineering
Metallurgical Thermodynamics and Modelling

Supervising professor
Professor Pekka Taskinen

Thesis advisor
Professor Pekka Taskinen

Preliminary examiners
Professor (Emeritus) Krzysztof Fitzner, Academy of Mining and Metallurgy, Cracow, Poland
Professor Gabriella Tranell, Norwegian University of Science and Technology, Trondheim, Norway

Opponents
Professor Evgeniy G. Osadchii, Russian Academy of Sciences, Institute of Experimental Mineralogy, Chernogolovka, Russia

Aalto University publication series
DOCTORAL DISSERTATIONS 5/2017

ISBN 978-952-60-7243-2 (printed)
ISBN 978-952-60-7242-5 (pdf)
ISSN-L 1799-4934
ISSN 1799-4934 (printed)
ISSN 1799-4942 (pdf)
http://urn.fi/URN:ISBN:978-952-60-7242-5

Unigrafia Oy
Helsinki 2017

Finland

Publication orders (printed book):
dmitry.sukhomlinov@aalto.fi

Author
Dmitry Sukhomlinov

Name of the doctoral dissertation
Thermodynamic properties of selected phases in the MgO-Sb-O, CaO-Te-O, Pt-Te-O, and Al_2O_3-Cu-O systems by the EMF method

Publisher School of Chemical Technology

Unit Department of Materials Science and Engineering

Series Aalto University publication series DOCTORAL DISSERTATIONS 5/2017

Field of research Processing of Materials

Manuscript submitted 21 October 2016 **Date of the defence** 3 February 2017

Permission to publish granted (date) 30 November 2016 **Language** English

☐ **Monograph** ☒ **Article dissertation** ☐ **Essay dissertation**

Abstract

Most of the non-ferrous metals are produced from sulfide ores. The high grade ores have been exhausted due to intensive consumption and increasing global demand of the metals. The available ores are getting poorer in metals and becoming increasingly more complex. Complexity of the primary raw materials is associated with continuously changing composition, presence of harmful impurities as well as valuable elements with significant concentrations. Furthermore, the secondary raw materials, such as various wastes of electrical and electronic equipment are very complex too.

Therefore, efficient processing of such materials, troubleshooting, improving, and developing of industrial processes requires carefully acquired thermodynamic properties for modelling equilibria of chemical reactions and the phase stabilities.

In this study, thermodynamic properties of selected phases in the MgO-Sb-O, CaO-Te-O, Pt-Te-O, and Al_2O_3-Cu-O systems were determined accurately by the solid state EMF method, applying the state-of-the-art equipment. Particular attention was paid to the accuracy and precision of temperature and EMF measurements in carefully arranged experimental galvanic cells.

The thermodynamic data reported in the present work should be of great interest for extractive metallurgy as well as for development of new composite and functional materials and product developing work in the field of energy technology, geochemistry and other materials science applications.

Keywords equilibrium, electrochemistry, oxygen concentration cells, solid electrolytes, Gibbs energy

ISBN (printed) 978-952-60-7243-2 **ISBN (pdf)** 978-952-60-7242-5

ISSN-L 1799-4934 **ISSN (printed)** 1799-4934 **ISSN (pdf)** 1799-4942

Location of publisher Helsinki **Location of printing** Helsinki **Year** 2017

Pages 97 **urn** http://urn.fi/URN:ISBN:978-952-60-7242-5

Preface

The research work presented in this doctoral thesis was carried out at Aalto University, School of Chemical Technology, Department of Materials Science and Engineering, Metallurgical Thermodynamics and Modelling (TDM) research group during the years 2012 – 2016.

I would like to express my deepest appreciation to my supervisor, Professor Pekka Taskinen. I am very thankful to Pekka not only to a great advisor and a team leader but also to a great person who inspired me and helped to muster professional skills and knowledge. I got very lucky when I joined TDM group. I wish to thank him for the opportunity to conduct this research and for the working atmosphere he created in TDM group.

The thesis was conducted with a financial support of HIVEN – a project of Tekes, the Finnish Funding Agency for Technology and Innovation. HIVEN project was also financially supported by Outotec (Finland) Oy and Boliden Harjavalta Oy. I am grateful to the Association of Finnish Steel and Metal Producers for the financial support. The Aalto CHEM grant and the grant from TES (Tekniikan Edistämissäätiö) given for the final stage of the doctoral work are also greatly acknowledged.

I wish to thank my coauthors in this research work, Dr. Markus Aspiala, Dr. Fiseha Tesfaye, M.Sc. Niko Hellstén, and Dr. Daniel Lindberg for their valuable contribution.

I appreciate useful discussions and suggestions concerning various challenges I had been facing in my doctoral research with Professor Michael Gasik, Professor (Emeritus) Lauri Holappa and Professor Rauf Hurman Eric.

My TDM colleagues, Hanna Viitala, Sönke Schmachtel, Petteri Piskunen, Joseph Hamuyuni, Kaisu Avarmaa, Rui Zhang, Longgong Xia, Imam Santoso and Lassi Klemettinen are acknowledged for their help and support, assistance in experiments and analyses, critical feedbacks and just for being great workmates.

I want to thank Petteri Halli for being my office mate, his sense of humor and scientific discussions.

Also I would like to thank the työpaja group for the technical support, and particularly Into for the help in building experimental setups.

Finally, I would like to thank my family and friends for inspiration and encouragement and my particular thank to Olga for her endless patience and support.

20.10.2016, Espoo
Dmitry Sukhomlinov

List of Publications

This doctoral dissertation consists of a summary of the following publications which are referred to in the text by their corresponding Roman numbers. Articles are appended to this compendium in the same sequence.

[I] D. Sukhomlinov, M. Aspiala, P. Taskinen, Thermodynamic study of MgO-Sb_2O_3 system and the stability functions of magnesium antimonite, Journal of Chemical Thermodynamics, 72 (2014) 71-76. DOI: 10.1016/j.jct.2013.12.032.

[II] D. Sukhomlinov, F. Tesfaye, P. Taskinen, Thermodynamic stability of Ca_3TeO_6 determined by a solid electrolyte EMF method, Thermochimica Acta, 615 (2015) 38-42. DOI: 10.1016/j.tca.2015.07.001.

[III] Dmitry Sukhomlinov, Pekka Taskinen, Thermodynamic properties of intermetallic PtTe determined by means of a solid electrolyte EMF method, Journal of Chemical Thermodynamics, 93 (2016) 19-23. DOI: 10.1016/j.jct.2015.09.007.

[IV] Dmitry Sukhomlinov, Fiseha Tesfaye, Niko Hellstén, Daniel Lindberg, Pekka Taskinen, Thermodynamic stability of solid phases in the system Cu-O-Al_2O_3 by means of the EMF and DSC-TGA techniques, Journal of Solid State Electrochemistry, ahead of print. DOI: 10.1007/s10008-016-3430-1.

Author's contribution

Publication I. Thermodynamic study of $MgO\text{-}Sb_2O_3$ system and the stability functions of magnesium antimonite

The author defined the research plan, conducted experimental work, analyzed experimental raw data with the assistance of Markus Aspiala, calculated the stability functions and wrote the first version of the manuscript under the supervision of Prof. Pekka Taskinen. Then, the author prepared the final version of the manuscript with input from the coauthors.

Publication II. Thermodynamic stability of Ca_3TeO_6 determined by a solid electrolyte EMF method

The author defined the research plan, conducted experimental work with the assistance of Fiseha Tesfaye, analyzed experimental raw data, calculated the stability functions and wrote the first version of the manuscript under the supervision of Prof. Pekka Taskinen. The final version of the manuscript was prepared by the author with input from the coauthors.

Publication III. Thermodynamic properties of intermetallic PtTe determined by means of a solid electrolyte EMF method

The author defined the research plan, conducted experimental work, analyzed experimental raw data, calculated the stability functions and wrote the manuscript under the supervision of Prof. Pekka Taskinen.

Publication IV. Thermodynamic stability of solid phases in the system $Cu\text{-}O\text{-}Al_2O_3$ by means of the EMF and DSC-TGA techniques

The author defined the research plan, designed and constructed EMF experimental setups, carried out the sample preparation work with the assistance of Niko Hellstén, conducted the EMF experiments and interpreted the results. The DSC-TGA experiments were conducted and interpreted by Fiseha Tesfaye and Daniel Lindberg. The author prepared the manuscript under the supervision of Prof. Pekka Taskinen with input from the coauthors.

Table of contents

Preface i
List of Publications iii
Author's contribution v
Table of contents 1
List of Abbreviations and Symbols 3
1 Introduction 5
1.1 Objective of the thesis 5
1.2 New scientific contribution 6
1.3 Practical application 6
1.4 Thesis outline 7
2 Background of the EMF method with solid electrolytes 9
2.1 Solid electrolytes with oxygen ion conductivity 9
2.1.1 High ionic conductivity 11
2.1.2 Ion transference number 12
2.2 Development of experimental galvanic cells incorporating solid oxide electrolytes 12
2.2.1 Reference electrode 13
2.2.2 Volume of the electrode compartments 13
2.2.3 Side reactions 13
2.2.4 Selection of electrometer, temperature control and the protective atmosphere 14
2.3 Electrochemistry of a generalized galvanic cell with a solid oxide electrolyte incorporated 14
2.4 Advantages of the EMF method: 15
2.5 Drawbacks of the EMF method: 16
3 Experimental section 17
3.1 Purity and sources of chemicals utilized 17
3.2 Synthesis of compounds 18

3.3 Analysis employed for synthesized samples 19
3.4 The electrochemical cells, electrodes and electrolytes 19
3.5 Design of the EMF setups employed 20
3.5.1 Apparatus employed for measurements of cells (a)-(c) 21
3.5.2 Setups employed for measurements of cells (d)-(g) 22
3.6 Temperature, pressure and EMF measurements 25
4 Results and discussions 27
4.1 MgO-Sb-O system 27
4.2 CaO-Te-O system 30
4.3 Pt-Te-O system 32
4.4 Al_2O_3-Cu-O system 34
5 Conclusions 41
6 References 43

List of Abbreviations and Symbols

Abbreviations

PGMs	platinum group metals
WEEE	waste electrical and electronic equipment
EMF	electromotive force
EPMA	electron probe micro-analysis
DTA	differential thermal analysis
DSC	differential scanning calorimetry
SEM	scanning electron microscopy
EDS	energy dispersive spectroscopy
TGA	thermogravimetric analysis
XRPD	X-ray powder diffraction
TZ	tetragonal zirconia
PSZ	partially stabilized zirconia
FSZ	fully stabilized zirconia
YSZ	yttria stabilized zirconia
MSZ	magnesia stabilized zirconia
CSZ	calcia stabilized zirconia

Symbols

s	solid
l	liquid
g	gas
σ_e	electronic conductivity
σ_i	ionic conductivity
t_i	ionic transference number
T	temperature
T_{tr}	phase transition temperature
P_{O2}	oxygen partial pressure
μ_{O2}	oxygen chemical potential
$\mu^{\circ}_{O_2}$	standard oxygen chemical potential
E	EMF of a galvanic cell
F	Faraday constant
R	universal gas constant
$\Delta_r G^{\circ}$	standard Gibbs energy of reaction
$\Delta_f G^{\circ}$	standard Gibbs energy of formation
$\Delta_{f(ox)} G^{\circ}$	standard Gibbs energy of formation from the component oxides

$\Delta H°_{tr}$	standard enthalpy of phase transition
$\Delta_f H°$	standard enthalpy pf formation
$\Delta_f S°$	standard entropy of formation
C_p	heat capacity at constant pressure

1 Introduction

Growth of global metal production causes exhaustion of high-grade ore deposits. Implication of poorer raw materials with more complex mineral compositions challenges the metal making processes. Particularly in copper smelting, such impurities as As, Sb, Bi, Pb, Se, Te, Zn, Cd are deleterious, causing process difficulties and environmental problems. On the other hand, impurities can be valuable byproducts if feasibly recovered with sufficient purity. Sb, Ga, Ge, In and platinum group metals (PGMs) were defined as critical materials for the EU in 2010 based on an economic importance and supply related risks, recycling rate and substitutability [1]. In 2014 these elements were shortlisted again [2]. Precious and PGMs are typically recovered as coproducts in the copper refining processes, however it is still a long way towards the highest utility of complex raw materials within the circular economy concept.

The importance of secondary raw materials in production of metals such as copper and lead, has been increasing drastically over the last decades. The typical raw materials utilized by secondary smelters are complex wastes of electrical and electronic equipment (WEEE). WEEE contains various materials and elements including non-ferrous metals (Cu, Pb, Al, etc.), precious metals, PGMs and also hazardous elements [3].

Predictive phase equilibrium calculations to design, improve, and troubleshoot diverse industrial processes require precise thermodynamic data [4]. These data can be acquired experimentally by methods like calorimetry, vapour pressure measurements, electrochemical methods, and phase equilibration. Calorimetry is a direct method to measure the heat effects, while the EMF is a superior method for activity measurements and determination of standard Gibbs energies of formation [5]. Meanwhile, the Gibbs energy of formation is the fundamental accurate index of thermodynamic stability [6], which is of a great importance in variety of applications, including extractive metallurgy, energy technology, geochemistry, and designing of new materials. Therefore, experimental studies are essential for providing data of thermodynamic properties to complete and improve already available information and to acquire new data.

1.1 Objective of the thesis

In the present thesis the MgO-Sb-O, CaO-Te-O, Pt-Te-O, and Al_2O_3-Cu-O systems were experimentally investigated. Prior to the present study, several experimental works and some computational studies [7-38] focused on these selected systems

have been conducted, however the thermodynamic data reported previously are either incomplete to some extent or scarce. Therefore, the objectives of this thesis were:

1. to determine precisely thermodynamic properties of selected phases in the chosen systems by experimental EMF method at various temperatures;
2. to investigate phase relations in these systems in various temperature and composition ranges;
3. to contribute new experimental data in the chosen systems and to reveal the discrepancy among the data reported in the previous studies.

1.2 New scientific contribution

The new scientific contribution obtained within this work comprises experimentally acquired data in the MgO-Sb-O, CaO-Te-O, Pt-Te-O, and Al_2O_3-Cu-O systems at various temperatures and determined thermodynamic properties of selected phases.

Particularly in the MgO-Sb-O system, a new set of measurement points was obtained experimentally by the EMF method and oxygen partial pressure of the phase domain MgO-$MgSb_2O_4$-Sb was measured in a wide temperature range. Furthermore, the standard Gibbs energy of formation of $MgSb_2O_4$ from the elements as well as from its component oxides was determined.

In the CaO-Te-O system, Ca_3TeO_6 phase was found capable of coexisting with CaO and Te in certain conditions. The standard Gibbs energy of formation of Ca_3TeO_6 was determined for the first time.

In the Pt-Te-O system, the standard Gibbs energy of formation of PtTe was determined for the first time in a wide temperature range with oxygen concentration galvanic cells. The enthalpy of fusion of TeO_2 was redetermined.

In the Al_2O_3-Cu-O system, the Gibbs energies of formation of Cu_2O, CuO, $CuAlO_2$ and $CuAl_2O_4$ were accurately determined with carefully assembled electrochemical cells.

1.3 Practical application

Accurately determined thermodynamic data are of great importance for extractive metallurgy. This information is an essential basis for design, improvement, and troubleshooting of diverse industrial metallurgical processes. Furthermore, it can be utilized in the development of novel composite and functional materials incorporating the complex oxides and intermetallics of the studied systems. Stability of such a product at elevated temperature and oxygen partial pressure can be predicted based on the obtained experimental data.

1.4 Thesis outline

This compendium comprises four articles published in peer-reviewed scientific journals, which are appended to this compendium [I-IV]. A background of the EMF method with oxygen concentration electrochemical cells for determination of oxygen chemical potentials at elevated temperature is presented in Chapter 2. The entire experimental procedure for acquiring thermodynamic properties of the selected substances is discussed in details in Chapter 3. Chapter 4 follows up with obtained results and their discussions. The conclusions concerning the research conducted are summarized in Chapter 5.

2 Background of the EMF method with solid electrolytes

All solid state materials naturally are mixed ionic-electronic conductors, or in other words in any material there are in principle nonzero electronic and ionic conductivities (σ_e and σ_i, respectively). However, certain materials exhibit high ionic and negligible electronic conductivities in certain conditions. Usually, materials in which σ_i exceeds σ_e by more than two orders of magnitude are considered as solid electrolytes [39].

Solid electrolytes have been known from 1830s when Michael Faraday observed electrical conductivity of lead fluoride at high temperature. And at the turn of XXth century, the high ionic conductivity of doped zirconia based on the transport of oxide ions was discovered by Walther Nernst [39].

Solid electrolytes can be classified based on the type of the conductor. The most practically useful and well known ones are stabilized zirconia and thoria based electrolytes (O^{2-} conductors), calcium fluoride and magnesium fluoride (F^- conductors), β- and β″-alumina types (conductors of various ions, such as Na^+, K^+, Li^+, Ag^+, Cu^+, etc.), silver iodide and rubidium silver iodide (Ag^+ conductors) [40].

Kiukkola and Wagner discussed and applied solid electrolytes in their pioneering studies [41 and 42] and their work initiated numerous electrochemical studies with galvanic cells based on solid electrolytes around the world. Since then, a wealth of thermodynamic data has been acquired with the solid state EMF method and advanced experimental techniques with solid electrolyte galvanic cells have been developed. With the EMF method it is possible to determine Gibbs energy, chemical potential, thermodynamic activity, or partial pressure values with superior accuracy and precision compared to the other thermodynamic experimental methods. Moreover, from the temperature dependence of the EMF, entropies and enthalpies of reactions can be calculated [43].

2.1 Solid electrolytes with oxygen ion conductivity

Solid electrolytes with oxygen ion conductivity have variety of applications such as oxygen sensors, fuel cells, oxygen pumps, electrochemical reactors and steam electrolysis cells. Besides that, galvanic cells incorporating solid electrolytes can be built for precise thermodynamic and kinetic measurements. For reliable determination of thermodynamic properties, utilized solid oxide electrolytes should meet certain requirements, i.e., high ionic conductivity, stability,

mechanical strength and toughness. Zirconia based electrolytes are the most widely used oxygen-ion conductors due to a good combination of high ionic conductivity and mechanical properties [44].

Pure zirconium dioxide (pure zirconia, ZrO_2) has three stable polymorphs. A monoclinic type of structure is stable at ambient conditions and up to 1370 K, above which it undergoes a phase transformation to a tetragonal form and then to a cubic form with the fluorite structure at 2643 K. Pure zirconia melts at 2988 K. [45]. The high temperature forms, i.e., the tetragonal and cubic ones can be stabilized at ambient temperature. It is normally achieved by a chemical doping with divalent (Ca^{2+}, Mg^{2+}) and trivalent (Y^{3+}, Sc^{3+}, Nd^{3+}) cations forming solid solutions. The doping results in the generation of oxygen ion lattice vacancies which are responsible for the ionic conductivity of these materials [46]. This process generates the stabilized tetragonal zirconia (TZ) and stabilized cubic zirconia. Depending on the amount of the dopant, it can be partially stabilized zirconia (PSZ), or fully stabilized zirconia (FSZ), if the amount of the dopant is sufficient. In these solid solutions the aliovalent dopant cations are located substitutionally on the host Zr^{4+} sites, while the overall electrical neutrality is achieved by incorporating the oxygen ion vacancies into the anion sublattice. The ionic conductivity of zirconia based solid electrolytes depends on the type of the dopant used, its concentration and phase assemblage occurring in the electrolyte. The maximum of the conductivity corresponds to the minimum amount of the dopant required to fully stabilize the fluorite phase. For yttria this amount is about 8-9 mol% [44], while for calcia or magnesia it is about 16 mol% [47].

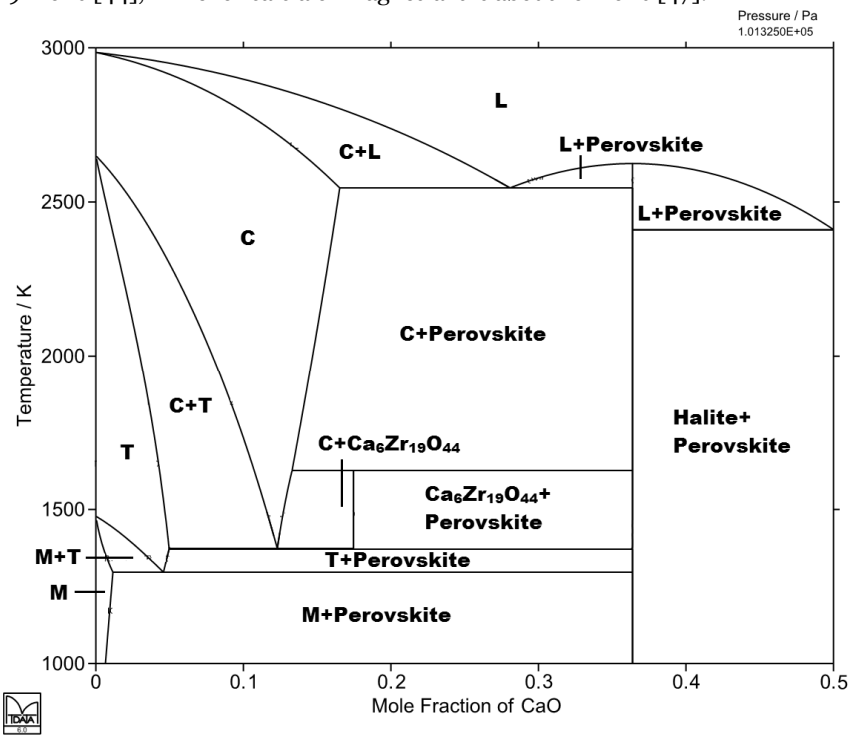

Figure 1. Computational ZrO_2-CaO pseudo-binary phase diagram (M, T, and C symbolize the monoclinic, tetragonal, and cubic phases, respectively; L symbolizes oxide liquid) [48].

Figure 1 illustrates the ZrO_2-CaO pseudo-binary phase diagram up to 0.5 mol fraction of CaO calculated based on MTOX database, version 8.2 [48]. Wide composition and temperature range of the cubic phase (the fluorite structure) can be seen in Figure 1.

Compared to thoria based solid electrolytes, stabilized zirconia electrolytes have better thermal shock resistance, and they are less expensive and commercially available in various shapes and dimensions. However, thoria based electrolytes are indispensable in low P_{O2} measurements.

2.1.1 High ionic conductivity

The values of partial ionic and electronic conductivities are of a great importance in choosing solid oxide electrolyte for high temperature thermodynamic measurements. These values for stabilized zirconia vary as a function of temperature, oxygen partial pressure, and its composition. Stabilized zirconia has been employed in multiple experimental thermodynamic studies and it is widely known as a solid electrolyte with pure ionic conductivity [46]. However, at low oxygen chemical potentials, an increased electronic conductivity of stabilized zirconia was reported [49] Therefore, in these conditions, solid electrolytes based on thoria can be utilized as a more convenient alternative. Figure 2 presents conductivity values for several solid oxide electrolytes as a function of temperature.

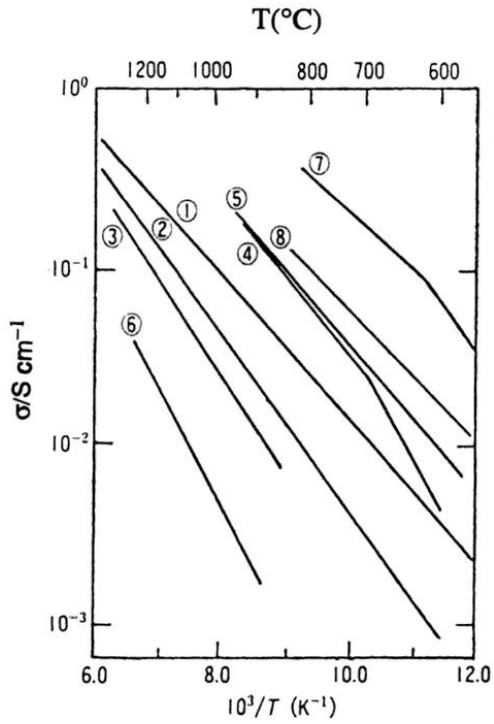

Figure 2. Conductivity for several oxygen ion conductors as a function of temperature: (1), 10 mol% Y_2O_3-ZrO_2; (2), 13 mol% CaO-ZrO_2; (3), 7 mol% Y_2O_3-ThO_2; (4), 20 mol% $GdO_{1.5}$-CeO_2; (5), 20 mol% $SmO_{1.5}$-CeO_2; (6), 12 mol% CaO-HfO_2; (7), 25 mol% Y_2O_3-Bi_2O_3; (8), 25 mol% WO_3-Bi_2O_3. [39].

These two types of oxide solid electrolytes, i.e., stabilized zirconia and thoria-based electrolytes complement each other and cover a wide range of oxygen partial pressures. The former exhibits pure ionic conductivity at higher P_{O2} (above 10^{-15} atm), while the latter is applicable in a rather reductive conditions, at lower P_{O2} (from 10^{-5} to 10^{-25} atm) [50]. Both types can be successfully applied in the intermediate range of oxygen partial pressures.

2.1.2 Ion transference number

For certain applications, particularly for fuel cells presence of some electronic conductivity can be tolerated, however in thermodynamic measurements, electronic conductivity is extremely harmful and the ion transference number should be greater than 0.99. Figure 3 presents electrolytic domain with $t_i \geq 0.99$ for several solid oxide electrolytes [51].

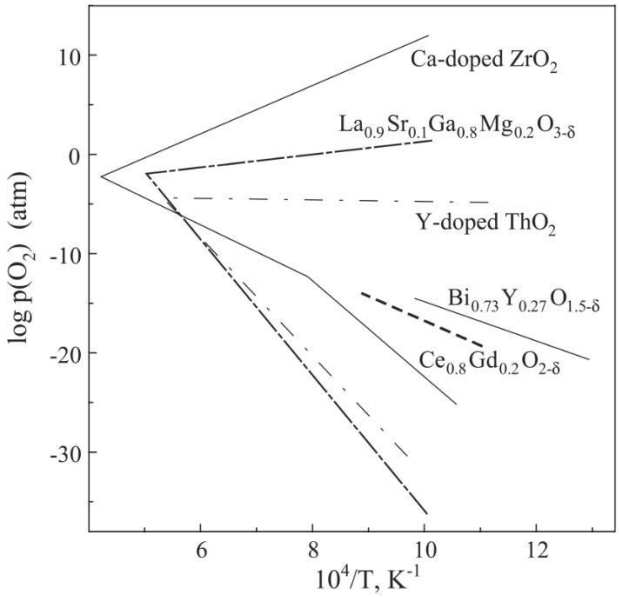

Figure 3. Low and high P_{O2} boundaries of the electrolytic domain ($t_i \geq 0.99$) for several oxygen ion conductors [51].

In Figure 3 the boundary lines show temperature and oxygen partial pressure applicability ranges of the electrolytes for thermodynamic measurements.

2.2 Development of experimental galvanic cells incorporating solid oxide electrolytes

Identification of a singular reversible process occurring at each electrode and usage of a suitable solid electrolyte type are primary tasks to be solved for a successful operation of a galvanic cell [52].

Multiple designs of oxygen concentration galvanic cells described in the literature can be generally classified into two groups. Simple cells comprised of solid electrodes and an electrolyte held together with a “sandwich structure” in a common protective gas atmosphere constitute the first group. Such a design is

applicable when equilibrium oxygen partial pressures of the electrodes are sufficiently low, and the chosen reference electrode should have equilibrium oxygen partial pressure similar to the test electrode under investigation. The obvious disadvantage of this arrangement is existing oxygen transfer via the common gas atmosphere. However, an appropriate insulation of the electrodes by a local sealing with alumina cement or high-melting glass can solve this problem.

The second group comprises galvanic cells with totally separated electrode compartments, where each electrode has its individual gas atmosphere. This arrangement requires a long gas-tight solid electrolyte tube. Thus, gaseous reference electrodes, such as pure oxygen, air, hydrogen / water vapor mixtures or carbon monoxide / carbon dioxide mixtures can be adapted.

Design of a future galvanic cell and an overall apparatus ultimately depends on the features of the studied thermodynamic system. Useful information which can help to design a suitable experimental setup includes an estimative oxygen partial pressure of the test electrode, partial pressures of volatile species in the system, reactivity of the studied substances with solid electrolyte and leads.

2.2.1 Reference electrode

Reference electrode should be selected in such a way that its equilibrium oxygen partial pressure does not go beyond the pure ionic conductivity range of the electrolyte used. Also, design related issues should be considered. If the galvanic cell is assembled in a simple open arrangement with a common gas atmosphere, then reference electrode should be selected in such a way that the difference in oxygen chemical potentials between the electrodes is minimized. Such a design can be successfully employed if the measured partial pressures are sufficiently low. If the electrode compartments are fully separated, then the primary pure oxygen reference electrode is preferable.

2.2.2 Volume of the electrode compartments

In the experimental arrangement of the galvanic cells, volume of the electrode compartments should be minimized, particularly when electrodes with rather high partial pressure are studied. This issue becomes less critical when the equilibrium P_{O_2} is rather low, but another difficulty may appear. Purity of commercially available argon gas can be insufficient and a certain purification procedure is required in order to prevent oxidation of the studying electrodes.

2.2.3 Side reactions

Reactions between electrodes and electrolyte, electrodes and lead wires, electrodes and crucibles used as a container must be avoided [52].

Stabilized zirconia is rather inert material, however electrodes, which contain certain reactive oxides may corrode the electrolyte. Particularly iron oxides are known to attack stabilized zirconia [53]. This phenomenon can be especially problematic if oxygen activity is measured in molten oxide systems.

Pure platinum wires are preferable to be utilized as leads, because they do not cause unknown thermovoltage, which would be the case if different lead wires are used. However, in certain cases, especially when the electrodes are fully or partially molten, Pt can react with electrodes reducing the measurement accuracy or even making the measurement impossible. This problem can be prevented if chemically inert material with sufficient electrical conductivity can be found and adapted as a contact material. Such materials as Rh, Ir, Mo, W, Re [54], Os, and graphite can be utilized for that purpose. However, the corresponding thermovoltage must be considered if the length of such a contact is significant.

2.2.4 Selection of electrometer, temperature control and the protective atmosphere

Electrometers with a high input impedance should be used for reversible open circuit measurement.

Temperature control should be at rather advanced level in order to minimize temperature fluctuations. Temperature gradient over the cell should be minimized by its location right in the hot zone of the furnace and by minimization of its mass and dimensions.

In certain cases, inert gas utilized as a protective atmosphere may require some purification. Such purification is especially important when electrodes with low equilibrium oxygen partial pressures are used, to ensure that the partial pressures are not altered by the cell surroundings. In this regard, various purification systems can be utilized, i.e., columns filled with active metals (Ti, Zr, Cu, Ba, Ca, etc.) with a high specific surface area at elevated temperatures [54].

Effect of external electromagnetic fields can be eliminated by employing a grounded Faraday cage.

2.3 Electrochemistry of a generalized galvanic cell with a solid oxide electrolyte incorporated

The reversible EMF (E / V) of a generalized galvanic cell (1) incorporating a solid oxide electrolyte can be expressed by Equation (2).

$$(-)\mathrm{Pt}|\mathrm{O_2(g)}, (\mathrm{P'_{O_2}})|\ \mathrm{O^{2-}\ conductor}|\mathrm{O_2(g)}, (\mathrm{P''_{O_2}})|\mathrm{Pt}(+), \qquad (1)$$

where $\mathrm{P'_{O_2}}$ and $\mathrm{P''_{O_2}}$ are the equilibrium oxygen partial pressures of the test (left hand side) and reference (right hand side) electrodes.

$$E = \frac{1}{4F}\int_{\mu'_{O2}}^{\mu''_{O2}} t_i \, d\mu_{O_2}, \qquad (2)$$

where μ'_{O2} and μ''_{O2} are the oxygen chemical potentials established at the test and reference electrodes, respectively, by condensed phase equilibria or by appropriate partial pressures of the gaseous component (O_2), ($\mu'_{O2} < \mu''_{O2}$). F stands for the Faraday constant (96485.3399 C mol^{-1}) [55].

The ionic transference number t_i can be expressed by:

$$t_i = \frac{\sigma_i}{\sigma_i + \sigma_e}. \quad (3)$$

Under normal conditions, when the solid electrolyte exhibits pure ionic conductivity or in other words its electronic conductivity is negligible (transference number t_i is assumed to be one), the EMF of cell (1) is given by Equation (4).

$$E = \frac{\Delta\mu_{O_2}}{4F} = \frac{(\mu''_{O_2} - \mu'_{O_2})}{4F}, \quad (4)$$

where $\Delta\mu_{O_2}$ is the difference of the oxygen chemical potential between the cell electrodes.

The oxygen chemical potential can be written in terms of the equilibrium oxygen partial pressure:

$$\mu_{O_2} = \mu^{\circ}_{O_2} + RT\ln P_{O_2}, \quad (5)$$

where $\mu^{\circ}_{O_2}$ is the standard oxygen chemical potential, R stands for the universal gas constant (8.314472 J mol^{-1} K^{-1}) [55] and T stands for the temperature (K).

Therefore, Equations (6) and (7) can be written:

$$E = \frac{RT}{4F}\ln\frac{P''_{O_2}}{P'_{O_2}}, \quad (6)$$

$$P'_{O_2} = P''_{O_2} \times e^{-\left(\frac{4EF}{RT}\right)}, \quad (7)$$

where P'_{O2} and P''_{O2} are the oxygen partial pressures of test and reference electrodes.

Equation (7) provides a simple relation between the cell EMF values measured at certain measured temperatures and the equilibrium oxygen partial pressures of the cell electrodes, while one of them is predominantly well known (reference electrode, P''_{O2}). Thus, the equilibrium oxygen partial pressure of the test electrode (P'_{O2}) can be calculated as a function of temperature.

2.4 Advantages of the EMF method:

- The measured EMF is directly related to investigating thermodynamic properties by a simple equation.
- Accuracy of the measured chemical potential and Gibbs energy is highest among the other experimental methods.
- Measurements are conducted at elevated temperature, therefore a real equilibrium is attainable.
- Experimental data are acquired in isothermal condition, or in other words, the EMF method is a static method, and the measured quantities practically do not vary with time when equilibrium is attained.

2.5 Drawbacks of the EMF method:

- The partial enthalpy and entropy are determined indirectly from EMF vs. temperature dependence, and often these values are less accurate than direct calorimetric measurements.
- Experimental work is demanding, time consuming and requires certain laboratory skills.
- Equilibration time can be extremely long in certain cases, especially at lower temperatures.

Method can be incapable if side reactions take place, such as reaction of electrodes with electrolyte or leads.

3 Experimental section

The experimental procedure employed in the present work is described in this chapter. It includes a list of utilized chemicals and synthesis procedure of certain compounds, analytical methods applied for the purity control and an arrangement of experimental EMF setups employed. Particular attention is paid to the accuracy and precision of the temperature, ambient pressure and EMF measurements. Important design features of the oxygen concentration galvanic cells used are illustrated.

3.1 Purity and sources of chemicals utilized

Tables 1 and 2 present, respectively, lists of chemicals and gases used in the present work with information of their purity and sources. All gases utilized in this work were supplied by AGA (Finland).

Table 1. Chemicals utilized in the present work, their form, purity and provenance.

Chemical	Form	Purity, wt%	Provenance
Al_2O_3	Powder	99.99	Sigma-Aldrich (USA)
CaO	Powder	99.9	Sigma-Aldrich (USA)
Cu	Ingots	99.996	Boliden Harjavalta Oy (Finland)
Cu	Powder	99.995	Alfa Aesar (Germany)
CuO	Powder	99.995	Alfa Aesar (Germany)
MgO	Powder	99.995	Sigma-Aldrich (USA)
Pt	Wire	99.99	Johnson-Matthey Noble Metals (UK)
Sb	Lumps	99.999	Cerac Inc., Milwaukee, Wisconsin (USA)
Sb_2O_3	Powder	99.995	Koch-Light Laboratories LTD (UK)
Te	Powder	99.999	Alfa Aesar (Germany)
TeO_2	Powder	99.99	Alfa Aesar (Germany)

Table 2. Gases utilized in the present work with their purity.

Gas	Purity, vol%
N_2	99.998
Ar	99.999
O_2	99.95 / 99.999

3.2 Synthesis of compounds

Magnesium antimonite ($MgSb_2O_4$) was synthesized from equimolar mixture of its component oxides, i.e., MgO and Sb_2O_3. The reactants in powder form were thoroughly mixed in an agate mortar and pressed into a pellet at a pressure of about 0.25 GPa. The pellet placed into an alumina crucible was heat-treated at 973 K for 24 h in a protective atmosphere of N_2. The completion of the reaction was confirmed by XRPD.

Calcium orthotellurate (Ca_3TeO_6) saturated with calcium oxide was synthesized from CaO and TeO_2. The starting powder mixture containing 57 mol% of CaO was pressed into a pellet and placed into a fused silica crucible with another protective pellet made of pure CaO at the bottom. The sample was heat-treated at 1000 K for 8 h in a protective atmosphere of Ar. After that the sample obtained was ground and mixed with an additional 25 mol% of CaO. This mixture was two time subjected to the same procedure of pelletizing and heat-treatment with following grinding. The heat-treatment was conducted in a protective atmosphere of Ar stepwise: 21 h at 1000 K, 0.25 h at 1173 K, and 21 h at 973 K. The composition of the sample obtained was confirmed by SEM-EDS and XRPD to be Ca_3TeO_6 with CaO saturation.

Intermetallic platinum monotelluride (PtTe) saturated with metallic platinum was synthesized in an evacuated fused silica ampoule from Te powder and 0.5 mm in diameter Pt wire cut in short pieces. The mixture containing about 40 at% Te was pressed into a pellet and put into the ampoule. The ampule was evacuated up to 2×10^{-2} mbar and then backfilled with Ar. This procedure was repeated 5 times in order to remove traces of reactive gases such as oxygen and then the evacuated ampoule was sealed with H_2/O_2 torch. The synthesis was performed stepwise: 16 h at 773 K, 1 h at 1173 K, and 23 h at 1073 K. The composition of the obtained sample was confirmed by SEM-EDS to be PtTe with Pt saturation.

Cuprous oxide (Cu_2O) was synthesized from cathode copper by oxidizing and subsequent quenching in air. The oxidation was conducted above 1299 K for 120 h and the composition of the sample quenched was examined by EPMA, confirming completion of cuprous oxide formation.

Copper aluminates, i.e., copper aluminate spinel ($CuAl_2O_4$) and cuprous aluminate delafossite ($CuAlO_2$) were synthesized by a ceramic route. Powders of Al_2O_3 and CuO were thoroughly mixed in an agate mortar with a molar ratio of 2:1, respectively. The mixture was pressed into a pellet and heat-treated at 1338 K for 24 h in air. This procedure with intermediate grinding and pelletizing was repeated three times for reaction completion. The formation of $CuAl_2O_4$ saturated with Al_2O_3 was confirmed by XRPD and SEM-EDS. The phase assemblage obtained was used as a starting material for preparation of $CuAlO_2$, i.e., $CuAl_2O_4$ saturated with Al_2O_3 was decomposed at 1473 K for 14 hours and cooled down to room temperature in a protective atmosphere of Ar. The formation of $CuAlO_2$ saturated with Al_2O_3 was confirmed by XRPD and SEM-EDS.

3.3 Analysis employed for synthesized samples

To ensure that desired compounds were synthesized successfully and the reactions were complete, the final products as well as certain intermediate samples were subjected to elemental composition and phase composition analyses.

In XRPD analysis the phase composition of a powdered specimen was examined by a PANalytical diffractometer (X'Pert Pro Powder, Almelo, Netherlands) equipped with CuKα radiation over a 2θ range of 10–70° at room temperature.

In SEM-EDS analysis, the elemental composition of each phase was examined. Before analysis, a specimen was mounted in an epoxy resin, then polished and carbon coated with a Leica EM SCD050 Coater (Leica Mikrosysteme GmbH, Wien, Austria). The polished section of the specimen was examined by a LEO 1450 (Carl Zeiss Microscopy GmbH, Jena, Germany) scanning electron microscope with a Link Inca X-Sight 7366 Energy EDS analyzer (Oxford Instruments plc, Abingdon, Oxfordshire, UK). The accelerating voltage used was 15 kV.

For EPMA, the specimen preparation procedure was the same as for SEM-EDS. The analysis was performed by CAMECA SX100 (Cameca SAS, France). The accelerating voltage of 15 kV and beam current of 40 nA were used in the analysis.

3.4 The electrochemical cells, electrodes and electrolytes

The synthesized samples ground into a power form with an agate mortar were mixed with additional components forming electrodes. Composition of the electrodes can be seen from the cell diagrams (a)-(g). Left hand side electrodes represent test electrodes and their phase compositions. Right hand side electrodes of cells (a)-(e) are gaseous pure oxygen reference electrodes, while cells (f) and (g) adopt biphasic solid mixtures formed in a similar way as test electrodes with agate mortar.

(−)Pt+Re | Sb(l)+MgO(s)+$MgSb_2O_4$(s) | YSZ | O_2(g) | Pt(+) (a)

(−)Pt+Ir/C | Te(l)+CaO(s)+Ca_3TeO_6(s) |YSZ | O_2(g) | Pt(+) (b)

(−)Pt | Pt(s)+PtTe(s)+TeO_2(s,l) | YSZ | O_2(g) | Pt(+) (c)

(−)Pt | Cu(s)+Cu_2O(s) | CSZ/YSZ | O_2(g) | Pt(+) (d)

(−)Pt | Cu_2O(s)+CuO(s) | CSZ/YSZ | O_2(g) | Pt(+) (e)

(−)Pt | Cu(s)+$CuAlO_2$(s)+Al_2O_3(s) | MSZ | Cu(s)+Cu_2O(s) | Pt(+) (f)

(−)Pt | $CuAl_2O_4$(s)+$CuAlO_2$(s)+Al_2O_3(s) | MSZ |
Cu_2O(s)+CuO(s) | Pt(+)* (g)

*Polarity changes at lower temperatures (EMF becomes negative).

Test electrodes of galvanic cells (a) and (b) contained a molten phase, i.e., antimony and tellurium, over entire experimental temperature range, thus the test electrodes were placed into YSZ solid electrolyte tube in a powder form. Meanwhile, test electrodes of cells (c)-(g) as well as reference electrodes of cells (f) and (g) were pressed into pellets. It was done to get reliable contacts between the electrolyte and solid electrodes with lead wires. Also, electrodes pressed in pellets facilitate faster equilibration.

In cell diagrams (a)-(g) abbreviations in between the electrodes symbolize solid oxide electrolytes, i.e., stabilized zirconia. In the present study, three different types of stabilized zirconia were employed. Table 3 presents solid electrolyte tubes and crucibles utilized in the conducted EMF experiments with their compositions and information about suppliers.

Table 3. Solid oxide electrolytes utilized in the present work.

Type	Composition	Provenance
YSZ	8.5 wt% Y_2O_3	Friatec (Germany)
CSZ	3.5 wt% CaO	Corning, Zircoa Products (Solon, USA)
MSZ	15 mol% MgO	Yamari (Japan)

At the ends of cell diagrams (a)-(g), materials utilized as leads and contacts are presented. Pt leads were used in all the cells, while contact materials are different. Pt contacts can be used directly to the electrode if a reaction between them is not expected, or it is kinetically slow and negligible, e.g., in solid state. However, in the presence of molten Sb and Te (cells (a) and (b), respectively), Pt wire can be rapidly attacked and should be protected from these molten and gaseous species. A short spot-welded tip of an inert metal or mechanically connected graphite rod can solve this problem. For Sb containing electrodes Re is a recommended contact material. Usage of Ir as a contact material for Te containing electrodes can be problematic in a long run, since there is a slow reaction which can gradually harm the accuracy of the measurement. However, graphite shows superior properties under these conditions.

3.5 Design of the EMF setups employed

Three individual setups were utilized in the present work. Two of them were vertically arranged and one was horizontal. An apparatus based on a vertical Lenton LTF 16/-/450 resistance tube furnace (Lenton, UK) was utilized to study thermodynamic stabilities of selected phases in the MgO-Sb-O, CaO-Te-O and Pt-Te-O systems (cells (a)-(c)). The Al_2O_3-Cu-O system was studied employing two other setups based on a vertical (type CSC 12/--/600V) and a horizontal (type CSC 12/--/600H) Lenton resistance tube furnaces (cells (d)-(g)). Table 4 presents amount of identical galvanic cells used with respective apparatus employed.

Table 4. Amount of experimental cells used and setups employed.

Cell type	Amount of identical cells used Apparatus employed		
	LTF 16/-/450	CSC 12/--/600V	CSC 12/--/600H
a	4	-	-
b	2	-	-
c	3	-	-
d	-	2	2
e	-	2	2
f	-	2	1
g	-	1	2

3.5.1 Apparatus employed for measurements of cells (a)-(c)

Figure 4 illustrates an apparatus based on a vertical Lenton LTF 16/-/450 resistance tube furnace (Lenton, UK) and various oxygen concentration cell arrangements employed are enlarged. Figure 5 illustrates the head of this vertical apparatus and arrangement of argon and oxygen flows.

Prior to the EMF measurements on the ternary systems, this setup was tested on rather well known oxides of tellurium, bismuth and antimony, i.e., TeO_2 [56], Bi_2O_3 [57], and Sb_2O_3 [58] in order to confirm absence of systematic errors. Furthermore, temperature dependences of $\Delta_fG°$ of TeO_2 and Sb_2O_3 were utilized in certain calculations presented in Chapter 4.

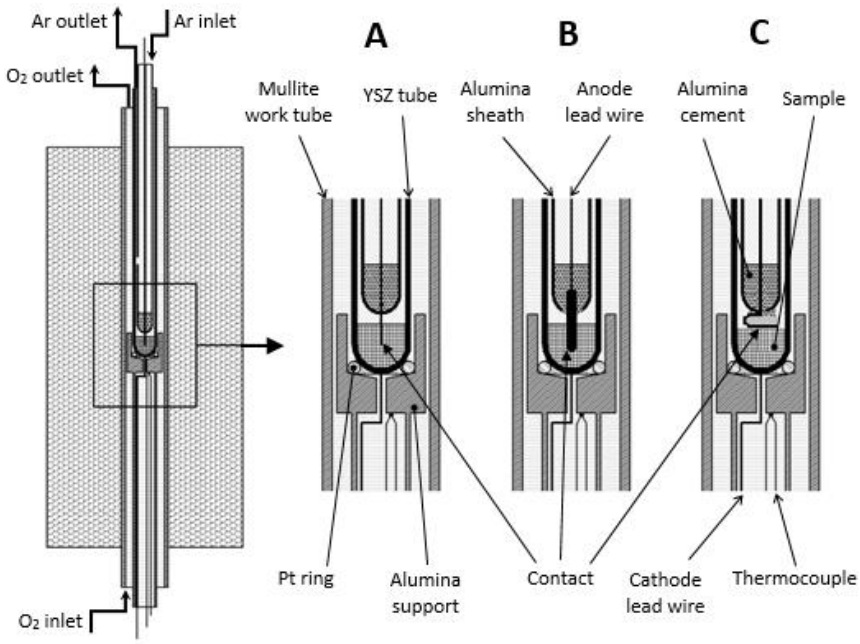

Figure 4. Vertical Lenton LTF 16/-/450 tube furnace and galvanic cell arrangements enlarged with various contact materials employed (A: Re or Ir contact; B: graphite contact; C: Pt contact).

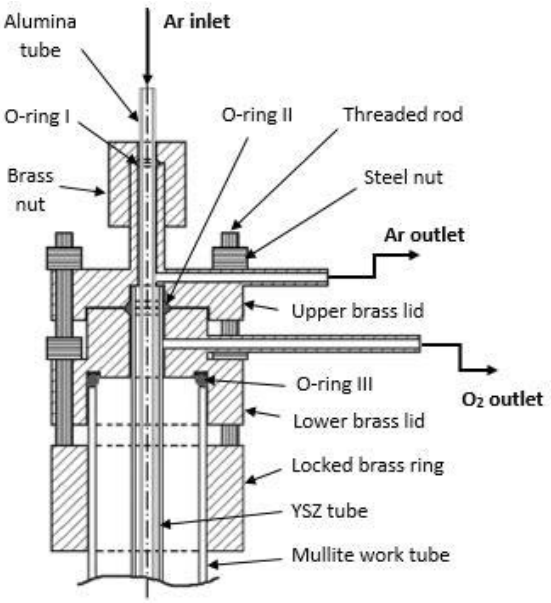

Figure 5. Head of vertical Lenton LTF 16/-/450 tube furnace illustrated schematically with emphasis on the arrangement of gas flows.

In a gas-tight mullite work tube (Figure 4 and 5) a steady oxygen flow was controlled by a digital mass flow controller, Aalborg DFC26 (USA). A solid electrolyte yttria stabilized zirconia tube inserted in the work tube separated the gaseous environments of the electrode compartments. The outer surface of the YSZ tube was flushed by a steady flow of the pure oxygen, while the cathode Pt lead wire tip shaped as a ring was pressed towards the round closed end of the YSZ tube, forming the reference electrode. In the test electrode compartment inside the YSZ tube, a nearly static protective atmosphere of argon was created in order to prevent oxidation of the test electrode. Argon was purified from its original purity by passing through titanium turnings at 873 K. The purified argon flow was controlled by a rotameter (Kytölä Muurame, Finland). Test electrode material, which was a mixture of three phases (see cell diagrams (a)-(c)) was placed inside the YSZ tube. In order to minimize temperature gradient over the cell the amount of the test electrode material was minimized to be less than 1 g. The contact between the anode Pt lead wire (or a contact material tip) and the test electrode was established at elevated temperatures by lowering the alumina sheath with the lead wire incorporated.

3.5.2 Setups employed for measurements of cells (d)-(g)

Prior to study thermodynamic properties of ternary compounds of the Al_2O_3-Cu-O system, measurements of rather well known thermodynamic stabilities of Cu_2O and CuO were conducted in order to evaluate reliability of the experimental setups employed. Furthermore, temperature dependences of $\Delta_fG°$ of Cu_2O and CuO were utilized in calculations presented in Chapter 4. Also, these data were needed

because of the choice of reference electrodes in cells (f) and (g). Experimental arrangements of cells (d)-(g) adapted in the vertical (type CSC 12/--/600V) and horizontal (type CSC 12/--/600H) Lenton resistance tube furnaces are illustrated in Figures 6 and 7, respectively. Whereas, the upper parts of Figures 6 and 7 show different experimental arrangements of cells (d) and (e), while the lower parts illustrate the arrangement of cells (f) and (g).

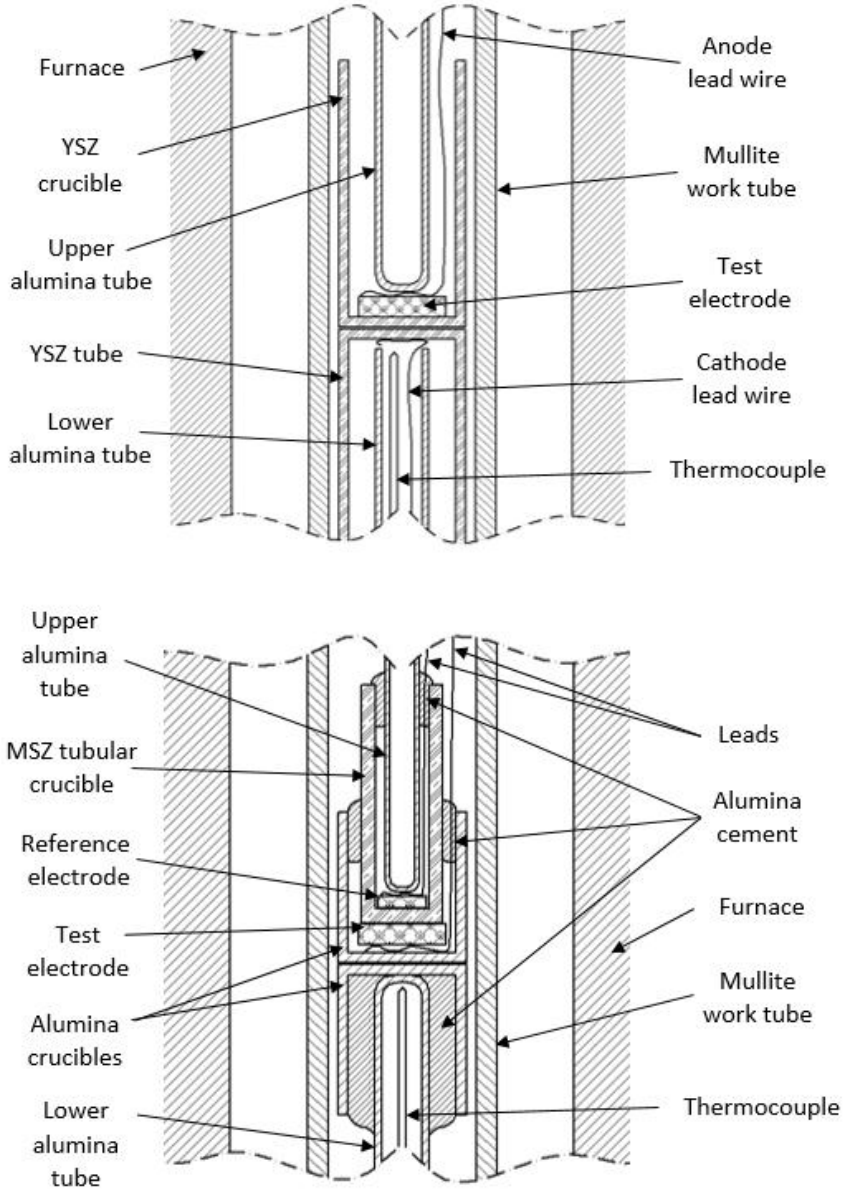

Figure 6. Experimental arrangement of galvanic cells (d)-(e) (upper one) and (f)-(g) (lower one) adapted in a vertical Lenton CSC 12/--/600V furnace.

The upper part of Figure 6 illustrates the assemblage of electrochemical cells (d)-(e) inside a mullite work tube. The reference electrode compartment was arranged in a long calcia stabilized zirconia tube with a closed flat end. A platinum

contact in a shape of a coil was pressed to the inner surface of the bottom of the CSZ tube by an alumina tube. Pure oxygen gas passed through this alumina tube and flushed the inner surface of the CSZ tube. Also, a calibrated S-type thermocouple was inserted into the alumina tube in such a way that its junction was located right next to the bottom of the solid electrolyte tube. The test electrode was arranged in a CSZ crucible. A pressed pellet made of either $Cu+Cu_2O$ (cell (d)) or Cu_2O+CuO (cell (e)) with a platinum contact was placed into the solid electrolyte crucible. And the crucible was placed on the CSZ tube (see the upper part of Figure 6), while the upper alumina tube pressed the whole assembly together providing perfect contacts on the interfaces. Both contacted CSZ surfaces were polished beforehand. The test electrode compartment was flushed with purified argon providing a nearly static protective atmosphere.

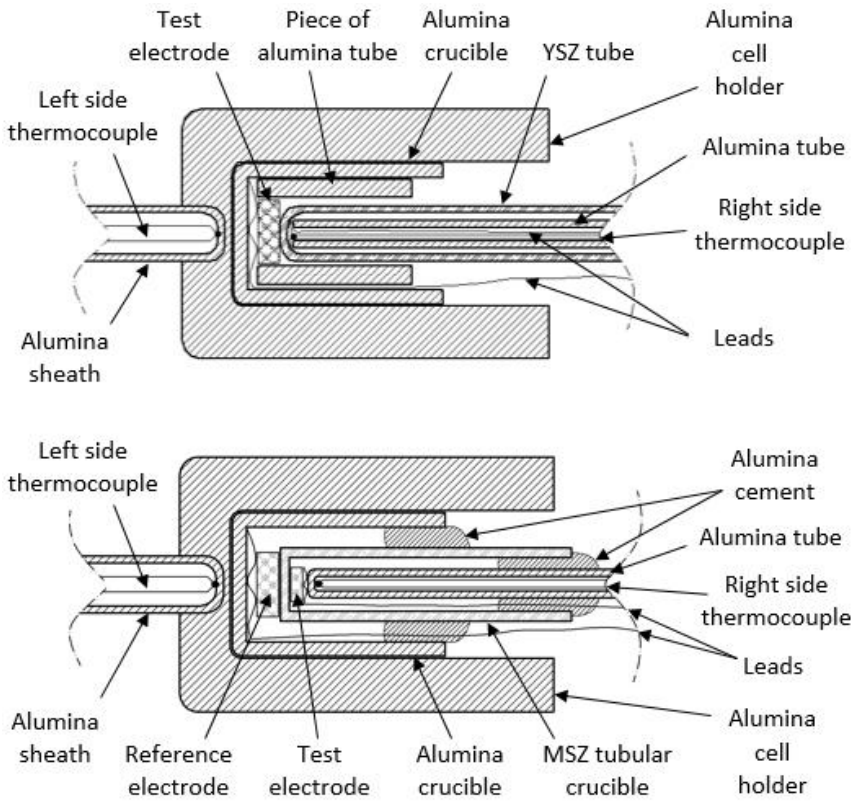

Figure 7. Experimental arrangement of galvanic cells (d)-(e) (upper one) and (f)-(g) (lower one) adapted in a horizontal Lenton CSC 12/--/600H furnace.

The upper part of Figure 7 shows the other experimental arrangement of electrochemical cells (d)-(e). The illustrated alumina sample holder was located inside a gas-tight fused silica work tube. The reference electrode was arranged inside a long YSZ tube by passing pure oxygen gas through an inserted alumina tube and flushing the inner surface of the YSZ tube. Also, this alumina tube pressed a tip of a Pt lead wire shaped as a coil to the inner surface of the bottom of the solid electrolyte tube, forming an electrical contact. The test electrode

pellets used in this setup were identical to those used in the vertical setup. The pellet with a Pt contact was pressed to the other side of the solid electrolyte tube. An alumina crucible and an alumina tube were utilized to support the test electrode pellet in the center of the alumina cell holder. The spring-loaded solid electrolyte tube pressed the pellet to the Pt contact, providing reliable contacts. Two S-type thermocouples were used to dispose the galvanic cell into the isothermal zone. One thermocouple was located in the alumina cell holder, the other one was inside the YSZ tube (see the upper part of Figure 7). The test electrode was protected by nearly static atmosphere of purified argon.

For galvanic cells (f) and (g) modified experimental arrangements depicted in the lower parts of Figures 6 and 7 were applied. These two arrangements are similar to each other, where solid reference and test electrodes were pelletized and pressed to the inner and other surfaces of the flat bottom of the MSZ tubular crucible. Tips of the Pt leads shaped as coils were incorporated to the electrodes and both electrode compartments were sealed with an alumina cement (see in the lower parts of Figures 6 and 7). Therefore, during the experiment each electrode was able to establish an equilibrium oxygen partial pressure inside its own electrode compartment. The cells were equilibrated in a nearly static atmosphere of purified argon.

Purification of argon was found to be critically important for the galvanic cells containing metallic copper. Gas was purified in two consecutive stages by passing it through chopped copper foil at 673 K (primary deoxidizing agent) and titanium turnings at 1173 K (secondary deoxidizing agent). In selected experiments the outgoing gas flow from the furnace was analyzed with an oxygen probe, Cambridge Sensotec Rapidox 2100 (UK) to ensure that protective atmosphere of argon gas was sufficiently purified.

For all studied galvanic cells (a)-(g), EMF measurements were performed in isothermal conditions. When an equilibrium was attained, the furnace temperature was changed. The reversibility of the cell EMF was checked in a heating and cooling cycles, as well as in repeated experiments with duplicate cells. Equilibration time varied from several hours to several days depending on the cell composition and temperature.

3.6 Temperature, pressure and EMF measurements

Temperature measurements were performed with calibrated S-type Pt-Pt/Rh thermocouples (Johnson-Matthey Noble Metals, UK) connected to a Keithley 2010 DMM multimeters (Keithley, USA). A Pt100 resistance thermometer (SKS-Group, Finland, tolerance class B 1/10) connected to a Keithley 2000 DMM multimeter was utilized as a cold junction compensation. Temperature was measured right next to galvanic cells and galvanic cells were located in the furnace hot zone, in such a way that temperature gradient over the cell was less than 1 K in all measurements. It was achieved either by furnace temperature profile measurement prior the experiment or by adjusting position of the cell during the measurement according to readings of two thermocouples located on the both sides of a cell.

Ambient pressure measurements were required when gaseous pure oxygen reference electrode was employed. Its normal value is 101325 Pa, however its natural fluctuation can be significant. If ignored, it can cause an error of determined $\Delta_r G°$ values up to several hundred J mol^{-1} in case of fluctuation within ± 2-3 % of the normal value. Oxygen gas utilized in arrangement of the reference electrode passed the reference electrode compartment of a galvanic cell and left the furnace through a bubbler. Therefore, the total pressure of the reference electrode was close to the ambient one. A small overpressure taking place on the reference electrode (several Pa) was measured with a Beamex MC2 calibrator (Finland) and incorporated with ambient pressure measured with a Vaisala PTU300 pressure, humidity and temperature transmitter (Finland) providing the actual total pressure on the reference electrode.

EMF measurements were performed with a Keithley 6517B electrometer connected to Pt lead wires (Johnson-Matthey Noble Metals, UK) of experimental galvanic cell. The utilized electrometer has a high input impedance of 2×10^{14} Ω and allows reversible EMF measurements in an open circuit [52]. All the measurements were simultaneously recorded with a computer over the entire experimental time.

4 Results and discussions

The results obtained in this study are presented in Appendices [I-IV] and summarized below. The standard Gibbs energy of formation of selected phases in the MgO-Sb-O, CaO-Te-O, Pt-Te-O, and Al_2O_3-Cu-O systems were determined experimentally by the EMF method with oxygen concentration galvanic cells.

The standard Gibbs energies of reactions (8)-(14) were calculated from experimental data measured in the present study.

$$2Sb(l) + MgO(s) + 3/2O_2(g) = MgSb_2O_4(s) \quad (8)$$

$$Te(l) + 3CaO(s) + 3/2O_2(g) = Ca_3TeO_6(s) \quad (9)$$

$$PtTe(s) + O_2(g) = TeO_2(s,l) + Pt(s) \quad (10)$$

$$2Cu(s) + 1/2O_2(g) = Cu_2O(s) \quad (11)$$

$$1/2Cu_2O(s) + 1/4O_2(g) = CuO(s) \quad (12)$$

$$Cu(s) + 1/2Al_2O_3(s) + 1/4O_2(g) = CuAlO_2(s) \quad (13)$$

$$CuAlO_2(s) + 1/2Al_2O_3(s) + 1/4O_2(g) = CuAl_2O_4(s) \quad (14)$$

4.1 MgO-Sb-O system

The standard Gibbs energy of reaction (8) is plotted as a function of temperature in Figure 8. A linear trend-line was fitted to the experimental data points applying the least-square method. Equation (15) describes the temperature dependence of the standard Gibbs energy of reaction (8) for the entire temperature range. The determination coefficient R^2 for the trend-line was calculated to be 0.9966.

$$\Delta_rG°/(kJ\ mol^{-1}) \pm 2.97 = -734.96 + 0.2645T/K. \quad (906 - 1148\ K) \quad (15)$$

Table 5 and Figure 8 present a comparison of the standard Gibbs energy of reaction (8) determined in this study and the results from the previous studies [7 and 8].

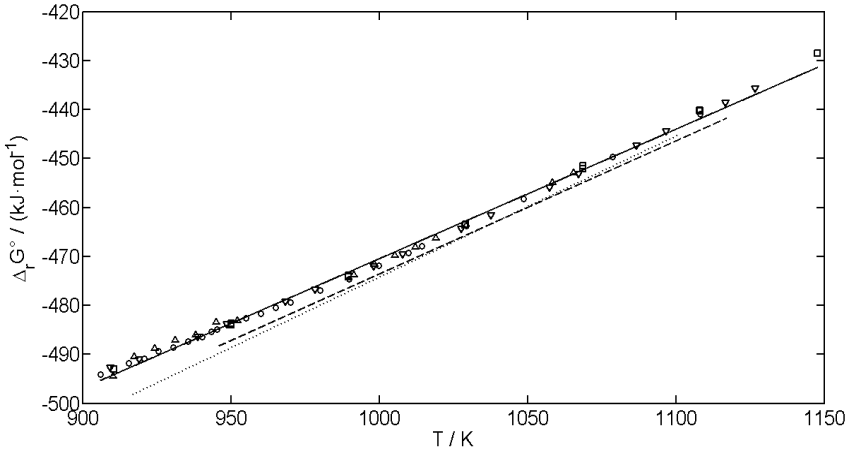

Figure 8. The standard Gibbs energy of reaction (8) as a function of temperature: (∇), cell I; (□), cell II; (○), cell III; (Δ), cell IV; (solid line), the least squares fitting; (dashed line), Katayama et al. [7]; (dotted line), Kemori et al. [8].

Table 5. The temperature dependence of the standard Gibbs energy of reaction (aa) determined in this work and compared to the results of the previous studies.

$\Delta_r G^\circ$ / (kJ mol^{-1})	T/K	Reference
-734.96+0.2645T/K	906 – 1148	This work
-745.6+0.2720T/K	945 – 1117	[7]
-762.2+0.2880T/K	917 – 1101	[8]

Figure 9 demonstrates a typical behavior of the galvanic cells employed in the heating and cooling cycles. Galvanic cell temperatures and EMF values measured are plotted as a function of time.

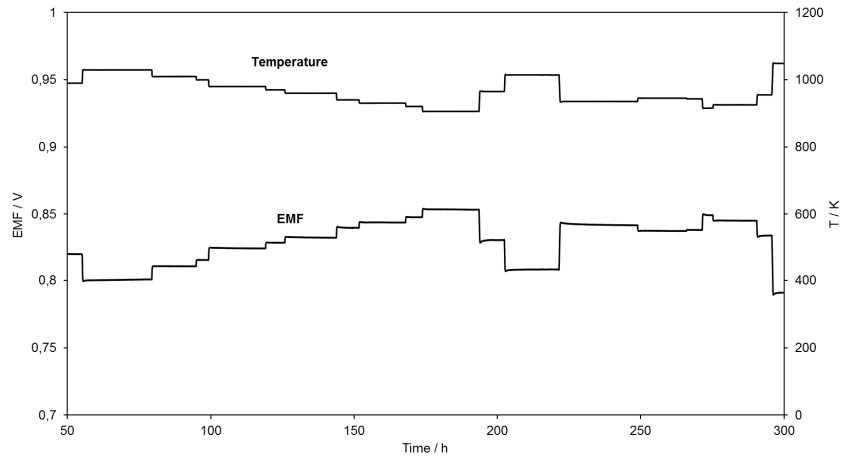

Figure 9. Typical behavior of experimental galvanic cells; EMF and temperature as a function of time.

The reaction of formation of magnesium antimonite $MgSb_2O_4$ from its component oxides can be written as:

$Sb_2O_3(l) + MgO(s) = MgSb_2O_4(s)$. (16)

The standard Gibbs energy of formation of $MgSb_2O_4$ from its component oxides according to reaction (16) was calculated by subtracting the standard Gibbs energy of formation of antimony trioxide Sb_2O_3 from the standard Gibbs energy of reaction (8). The standard Gibbs energy of formation of Sb_2O_3 was measured earlier, using a solid-oxide electrolyte EMF technique as follows [58]:

$\Delta_f G^\circ_{Sb_2O_3}/(kJ\ mol^{-1}) \pm 0.419 = - 682.21 + 0.2392T/K.$ (929 – 1080 K) (17)

Therefore, the standard Gibbs energy of formation of $MgSb_2O_4$ from its component oxides according to reaction (16) is expressed in Equation (18) and compared to results of the previous studies [7-9] in Table 6.

$\Delta_{f(ox)} G^\circ_{MgSb_2O_4}/(kJ\ mol^{-1}) \pm 3.00 = - 52.75 + 0.0253T/K.$ (929 – 1148 K) (18)

Table 6. The temperature dependence of the standard Gibbs energy of formation of $MgSb_2O_4$ from its component oxides determined in this work and compared to the previous studies.

$\Delta_{f(ox)}G^\circ$ / (kJ mol^{-1})	T/K	Reference
-52.75+0.0253T/K	929 – 1148	This work
-58.0+0.0287T/K	945 – 1117	[7]
-78.9+0.0495T/K	929 – 1101	[8]
-23.32-0.00068T/K	1173 – 1276.5	[9]

The results obtained are in a good agreement with the data reported previously in the literature. The $\Delta_{f(ox)}G^\circ$ value determined in this study at 1050 K is – 26.19 ± 3.00 kJ mol^{-1}, which is consistent with the values of –27.9 ± 1.1 kJ mol^{-1} and – 26.9 ± 0.7 kJ mol^{-1} measured by Katayama et al. [7] and Kemori et al. [8], respectively. At lower temperatures the scatter is higher. The EMF measurements with galvanic cells based on magnesium fluoride conducted by Raghavan [9] at higher temperatures yielded $\Delta_{f(ox)}G^\circ$ values nearly temperature independent . Thus, in the vicinity of 1050-1100 K, the results of this study agree well with Raghavan's, if extrapolated to these temperatures.

The reaction of formation of magnesium antimonite $MgSb_2O_4$ from the elements is given by:

$Mg(l) + 2Sb(l) + 2O_2(g) = MgSb_2O_4(s)$. (19)

The standard Gibbs energy of formation of $MgSb_2O_4$ was calculated as a sum of the standard Gibbs energy of reaction (8) and the standard Gibbs energy of formation of magnesium oxide MgO.

The standard Gibbs energy of formation of MgO determined with a chemical equilibrium technique was reported by Ono et al. [59] as follows:

$$\Delta_f G^\circ_{MgO}/(kJ\ mol^{-1}) \pm 18 = -657 + 0.141T/K. \quad (973 - 1323\ K) \quad (20)$$

Therefore, the standard Gibbs energy of formation of $MgSb_2O_4$ from the elements according to reaction (19) was calculated to be:

$$\Delta_f G^\circ_{MgSb_2O_4}/(kJ\ mol^{-1}) \pm 18.2 = -1392 + 0.4055T/K. \quad (973 - 1148\ K) \quad (21)$$

It appears to be the first report of $\Delta_f G^\circ_{MgSb_2O_4}$.

4.2 CaO-Te-O system

The temperature dependence of the standard Gibbs energy of reaction (9) is plotted in Figure 10, including the values of $\Delta_r G^\circ$ calculated from the measured experimental data point and the least-squares fitting. Equation (22) describes the linear regression best fit with the determination coefficient $R^2 = 0.9986$.

$$\Delta_r G^\circ/(kJ\ mol^{-1}) \pm 0.32 = -684.52 + 0.27026T/K. \quad (850 - 949\ K) \quad (22)$$

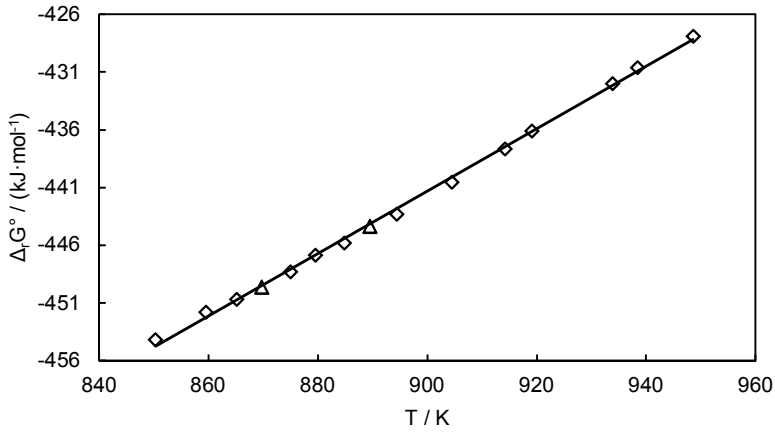

Figure 10. The standard Gibbs energy of reaction (9) as a function of temperature: (Δ), cell I; (◊), cell II; (solid line), the least squares fitting.

The standard Gibbs energy of formation of Ca_3TeO_6 from the elements according to reaction (23) was calculated as a sum of the standard Gibbs energy of reaction (9) and the standard Gibbs energy of formation of calcium oxide CaO times three.

$$3Ca(s) + Te(l) + 3O_2(g) = Ca_3TeO_6(s). \quad (23)$$

The standard Gibbs energy of formation of CaO was calculated from Gibbs energies of the pure substances taken from the SGTE database [60] to be:

$$\Delta_fG^\circ_{CaO}/(kJ\ mol^{-1}) = -634.40 + 0.1040T/K. \quad (750 - 1100\ K) \quad (24)$$

The $\Delta_fG^\circ_{Ca3TeO6}$ obtained is expressed in Equation (25) as a function of temperature:

$$\Delta_fG^\circ_{Ca_3TeO_6}/(kJ\ mol^{-1}) = -2587.73 + 0.58227T/K. \quad (850 - 949\ K) \quad (25)$$

This appears to be the first report of the thermodynamic stability function of calcium orthotellurate ($\Delta_fG^\circ_{Ca3TeO6}$) at elevated temperatures.

The standard enthalpy of formation of Ca_3TeO_6 at 298.15 K was estimated by Sahu et al. [61] to be -2474.6 kJ mol^{-1}. In order to compare the results of the present study with this estimate reported, the heat capacity of calcium orthotellurate was estimated by applying Neumann-Kopp rule [62]. For the estimation of the heat capacity of calcium orthotellurate the following hypothetical reaction was considered:

$$TeO_3(s) + 3CaO(s) = Ca_3TeO_6(s). \quad (26)$$

The estimated C_p as a function of temperature of Ca_3TeO_6 is expressed in Equation (27), which was calculated based of the heat capacity of CaO taken from the SGTE database [60] and the heat capacity of TeO_3 estimated by Sahu et al. [61].

$$C_p/(J\ mol^{-1}\ K^{-1}) = 261.336 - 19.527\cdot10^{-3}\ T/K - 60.5\cdot10^{5}\ (T/K)^{-2} + 15.993\cdot10^{-6}\ (T/K)^{2}. \quad (27)$$

By applying the second law method, the standard enthalpy and entropy of formation of Ca_3TeO_6 at 298.15 K were calculated utilizing Equations (28) and (29):

$$\Delta_fH^\circ_{298} = \Delta_fH^\circ_{mean} - \int_{298}^{Tmean} \Delta_fC_p dT + \sum \Delta H^\circ_{tr}, \quad (28)$$

$$\Delta_fS^\circ_{298} = \Delta_fS^\circ_{mean} - \int_{298}^{Tmean} (\Delta_fC_p/T) dT + \sum (\Delta H^\circ_{tr}/T_{tr}), \quad (29)$$

where $\Delta_fH^\circ_{mean}$ and $\Delta_fS^\circ_{mean}$ stand for the corresponding values determined in the linear relationship (25) and T_{mean} corresponds to the appropriate average value for all measurement points over the experimental temperature range (850 – 949 K). ΔH°_{tr} and T_{tr} are enthalpy change of a phase transition of a substance

involved into formation of Ca_3TeO_6 and temperature of the respective phase transition.

The heat capacities of pure elements (Ca, Te and O_2) taken from Barin and Knacke thermodynamic compilations [63] and the estimated heat capacity of Ca_3TeO_6 (Equation (27)) were integrated from the standard temperature up to 895 K (T_{mean}), taking into account the stoichiometric coefficients of the formation reaction. The enthalpy of fusion of Te and α-β phase transition of Ca were taken from Barin and Knacke thermodynamic compilations [63] and considered in the calculation.

The values calculated from Equations (28) and (29) are: $\Delta_f H°_{298}$ = -2577.53 kJ mol^{-1} and $\Delta_f S°_{298}$ = -571.67 J mol^{-1} K^{-1}. The enthalpy of formation of Ca_3TeO_6 at 298.15 K estimated by Sahu et al. [61] to be -2474.6 kJ mol^{-1} is in a fair agreement with the value calculated in this study from experimental results measured at elevated temperatures.

4.3 Pt-Te-O system

The standard Gibbs energy of reaction (10) is plotted as a function of temperature in Figure 11. Linear trend-lines were fitted to the experimental data points acquired below the melting point of tellurium dioxide TeO_2 and above it, by applying the least-square method. Equations (30) and (31) describe the temperature dependences of the standard Gibbs energy of reaction (10) for the different temperature ranges.

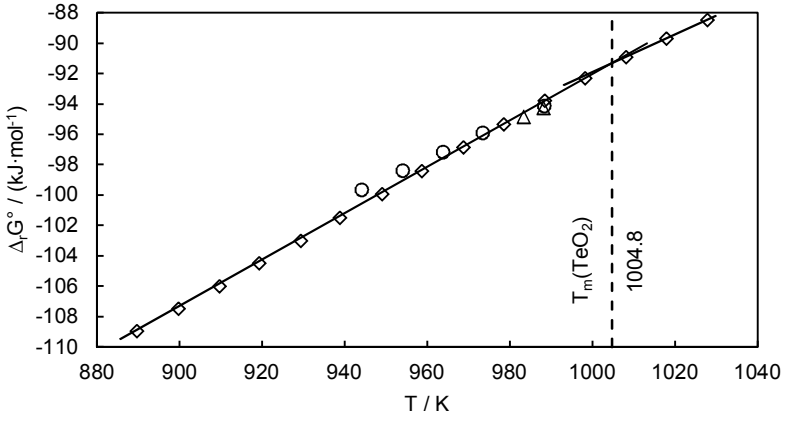

Figure 11. The standard Gibbs energy of reaction (10) as a function of temperature: (Δ), cell I; (○), cell II; (◊), cell III; (solid line), the least squares fitting; (dashed line) shows the tellurium dioxide melting point.

For the temperature range below the melting point of TeO_2, the following expression with the determination coefficient R^2 = 0.9954 was obtained:

$$\Delta_r G°/(\text{kJ mol}^{-1}) \pm 0.38 = -244.47 + 0.15243T/\text{K}. \quad (890 - 998\ \text{K}) \qquad (30)$$

For the temperatures above the TeO_2 melting point, only three measurement data points were acquired and the best least-squares fit with the determination coefficient $R^2 = 0.999998$ is described by Equation (31):

$$\Delta_rG°/(kJ\ mol^{-1}) \pm 0.50 = -215.33 + 0.12343T/K. \quad (1008 – 1028\ K) \qquad (31)$$

In Figure 11, a noticeable slope change of the $\Delta_rG°$ at the melting point of TeO_2 shown as the vertical dashed line can be observed. This change in slope is associated with the enthalpy of fusion of tellurium dioxide, which was calculated from Equations (30) and (31) to be $\Delta_{fus}H°_{TeO_2} = 29.14 \pm 2.40 kJ\ mol^{-1}$. It is in a good agreement with the value 29.079 kJ mol^{-1} recommended in the literature [64]. The melting temperature of TeO_2 calculated from Equations (30) and (31) is 1004.8 ± 21.7 K. This indirectly determined melting point agrees well with the literature value measured by a direct method, 1005.8 ± 1.0 K [65 and 66].

The standard Gibbs energy of formation of platinum monotelluride PtTe according to reaction (32) can be calculated by subtracting the standard Gibbs energy of reaction (10) from the standard Gibbs energy of formation of tellurium dioxide TeO_2.

$$Pt(s) + Te(l) = PtTe(s) \qquad (32)$$

The standard Gibbs energy of formation of TeO_2 was determined by the EMF method with oxygen concentration galvanic cells [56] to be:

$$\Delta_fG°_{TeO_2}/(kJ\ mol^{-1}) \pm 0.308 = -318.01 + 0.1810T/K. \quad (722.15 – 1005.8\ K) \qquad (33)$$

Therefore, the standard Gibbs energy of formation of PtTe according to reaction (32) was calculated as:

$$\Delta_fG°_{PtTe}/(kJ\ mol^{-1}) \pm 0.49 = -73.54 + 0.02857T/K. \quad (890 – 998\ K) \qquad (34)$$

This appears to be the first report of the $\Delta_fG°_{PtTe}$ data determined at high temperatures. Taking into account the enthalpy of fusion of tellurium $\Delta_{fus}H°_{Te}$ = 17.376 kJ mol^{-1} at 722.66 K [67], the high temperature data were extrapolated to low temperatures by using Equation (35).

$$\Delta_{tr(fus)}G° = \Delta_{tr(fus)}H° - (\Delta_{tr(fus)}H° / T_{tr(fus)})\ T. \qquad (35)$$

$$Pt(s) + Te(s) = PtTe(s) \qquad (36)$$

Therefore, the standard Gibbs energy of formation of PtTe according to reaction (36) was calculated as:

$\Delta_f G°_{PtTe}/(kJ\ mol^{-1}) \pm 0.49 = -56.16 + 0.00453T/K.$
(298.15 – 722.66 K) (37)

The standard enthalpy of formation of PtTe determined calorimetrically by Stolyarova and Osadchii [16] as -(56.52 ± 0.85) kJ mol^{-1} is in a good agreement with the result of the present study, -56.16 kJ mol^{-1}.

4.4 Al_2O_3-Cu-O system

The standard Gibbs energies of reactions (11) and (12) are depicted in Figures 12 and 13, respectively. The calculated best linear fits with determination coefficient R^2 of 0.9947 and 0.9882, respectively, are expressed in Equations (38) and (39). Comparison of the determined stability functions to the selected previous studies as well as experimental measurement data points are also provided in Figures 12 and 13.

$\Delta_r G° / (kJ\ mol^{-1}) \pm 0.511 = -170.089 + 0.074635T/K.$
(1003 – 1322 K) (38)

$\Delta_r G° / (kJ\ mol^{-1}) \pm 0.422 = -64.604 + 0.046670T/K.$
(907 – 1232 K) (39)

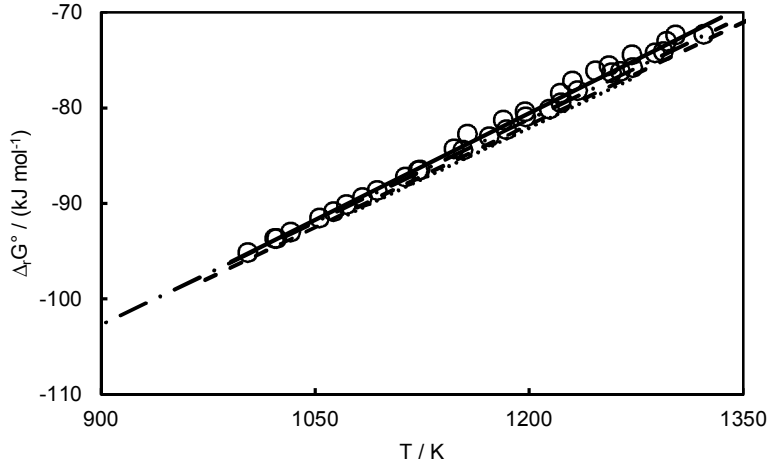

Figure 12. The standard Gibbs energy of reaction (11) as a function of temperature: (○), experimental measurement points; (solid line), the least squares fitting; (dashed line), Jacob and Alcock [68]; (dotted line), Slobodyanyuk et al. [69]; (dash-dotted line), Holmes et al. [70].

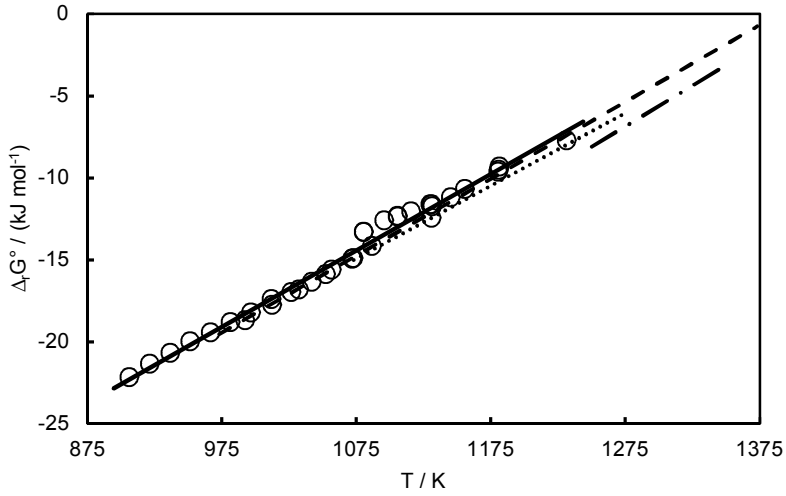

Figure 13. The standard Gibbs energy of reaction (12) as a function of temperature: (○), experimental measurement points; (solid line), the least squares fitting; (dashed line), Jacob and Alcock [68]; (dash-dotted line), Gadalla and White [71]; (dotted line), Slobodyanyuk et al. [69].

Figures 12 and 13 show an excellent agreement of the results obtained in this study with the previous experimental and computational studies [28, 68-71]. These measurements confirm reliability of the existing thermodynamic properties determined for cupric and cuprous oxides.

The standard Gibbs energies of reactions (13) and (14) determined are plotted in Figures 14 and 15 as a function of temperature with the best linear fits calculated and compared to the previous experimental studies. The calculated best linear fits are expressed in Equations (40) and (41). The determination coefficients R^2 are 0.9742 and 0.9901, respectively.

$$\Delta_r G^\circ / (\text{kJ mol}^{-1}) \pm 0.672 = -128.826 + 0.067854T/\text{K}. \quad (1051 - 1265\ \text{K}) \qquad (40)$$

$$\Delta_r G^\circ / (\text{kJ mol}^{-1}) \pm 0.158 = -39.225 + 0.024289T/\text{K}. \quad (1074 - 1262) \qquad (41)$$

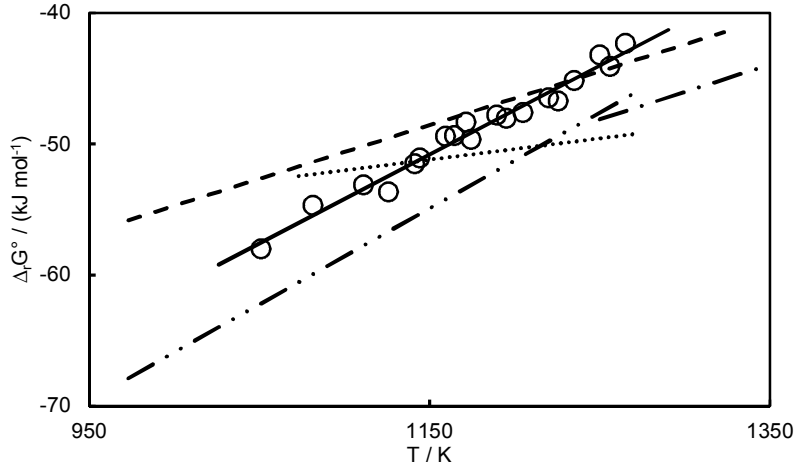

Figure 14. The standard Gibbs energy of reaction (13) as a function of temperature: (○), experimental measurement points; (solid line), the least squares fitting; (dashed line), Jacob and Alcock [68]; (dash-dotted line), Gadalla and White [71]; (dash-double-dotted line), Zalazinskii et al. [72]; (dotted line), Slobodyanyuk et al. [69].

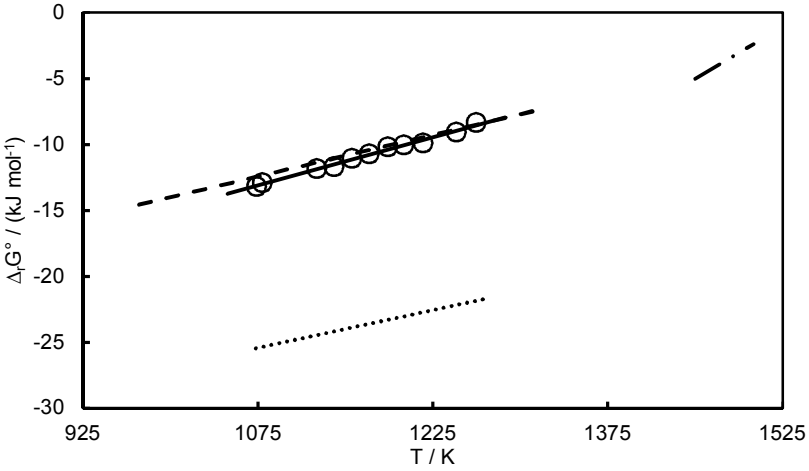

Figure 15. The standard Gibbs energy of reaction (14) as a function of temperature: (○), experimental measurement points; (solid line), the least squares fitting; (dashed line), Jacob and Alcock [68]; (dash-dotted line), Gadalla and White [71]; (dotted line), Slobodyanyuk et al. [69].

For the standard Gibbs energy of reaction (13), a significant scatter among the results of the previous studies can be seen in Figure 14. Partially it can be explained by the different experimental methods used in these studies. The $\Delta_r G°$ values measured in the previous studies at 1150 K do not differ from the present results for more than 4.2 kJ mol^{-1}, but the discrepancy increases at lower and higher temperature due to the differences in the slope. Therefore, the extrapolation can cause a significant error and should be avoided.

The standard Gibbs energy of reaction (14) measured electrochemically in the present work is in a good agreement with the EMF results reported by Jacob and Alcock [68] as can be seen in Figure 15. The TGA results reported by Gadalla and White [71] were measured only in a narrow temperature range, and therefore the slope is not reliable. However, if $\Delta_r G^\circ$ measured in this study is extrapolated to the higher temperature, it is in a good agreement with [71]. The results reported by Slobodyanyuk et al. [69] are significantly more negative and probably less accurate, due to an unknown systematic error in their EMF measurements.

Using the results of the present study the oxygen potential diagram for the system Cu-Al-O was derived at the temperature 1323 K and presented in Figure 16.

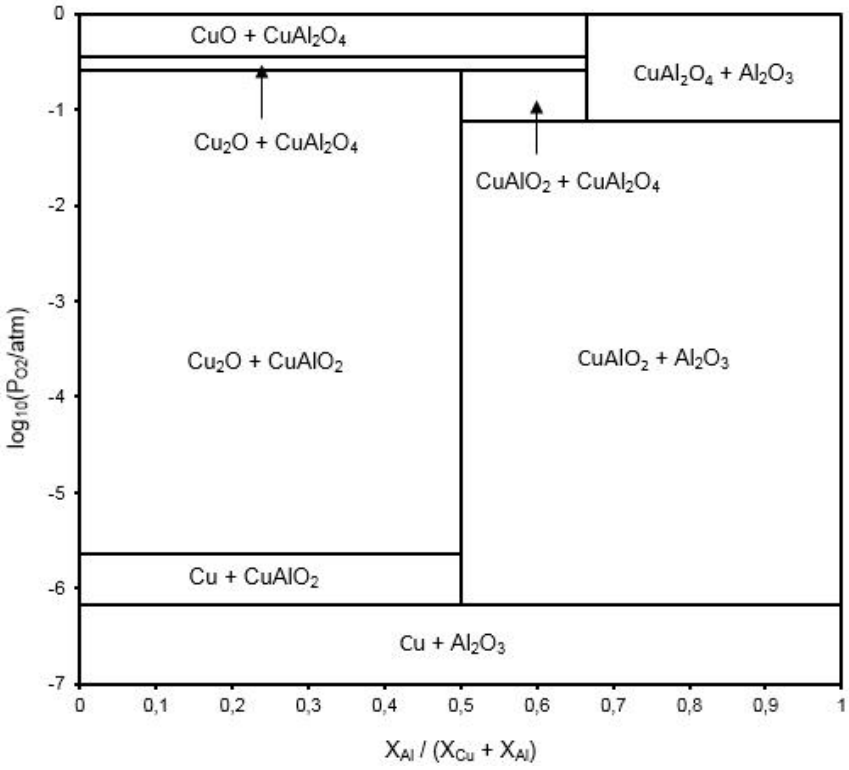

Figure 16. The Cu-Al-O stability diagram at 1323 K.

From the experimentally measured standard Gibbs energies of reactions (11) – (14) expressed in Equations (38) – (41), the standard Gibbs energies of formation of copper oxides from the elements and of copper aluminates from their component oxides can be calculated.

The standard Gibbs energy of formation of Cu_2O actually matches with the standard Gibbs energy of reaction (11):

$$\Delta_f G^\circ_{Cu2O} / (\text{kJ mol}^{-1}) \pm 0.511 = -170.089 + 0.074635T/\text{K}. \quad (1003 - 1322\ \text{K}) \qquad (42)$$

The standard Gibbs energy of formation of CuO was calculated as a sum of the standard Gibbs energy of reaction (12) and half of $\Delta_f G°_{Cu2O}$:

$$\Delta_f G°_{CuO} / (\text{kJ mol}^{-1}) \pm 0.663 = -149.649 + 0.083988T/K \quad (1003 - 1232\ K) \qquad (43)$$

The standard Gibbs energies of formation of Cu_2O and CuO are in a good agreement with the previous studies as well as with the values reported in the thermodynamic compilations [73].

The standard Gibbs energy of formation of $CuAlO_2$ from its component oxides can be calculated by subtracting half of $\Delta_f G°_{Cu2O}$ from the standard Gibbs energy of reaction (13) or simply from the measured EMF with galvanic cell (f) according to Equation (44).

$$\Delta_{f(ox)} G°_{CuAlO_2} = -FE_{cell\ (f)}. \qquad (44)$$

The standard Gibbs energy of formation of $CuAl_2O_4$ from its component oxides can be calculated by subtracting $\Delta_f G°_{CuO}$ from a sum of the standard Gibbs energies of reactions (13) and (14) or simply from the measured EMF with galvanic cell (f) and (g) according to Equation (45).

$$\Delta_{f(ox)} G°_{CuAl_2O_4} = -F(E_{cell\ (f)} + E_{cell\ (g)}). \qquad (45)$$

Therefore, the standard Gibbs energies of formation of copper aluminates from their component oxides are expressed by Equations (46) and (47):

$$\Delta_{f(ox)} G°_{CuAlO_2} / (\text{kJ mol}^{-1}) \pm 0.844 = -43.78 + 0.03054T/K, \quad (1051 - 1265\ K) \qquad (46)$$

$$\Delta_{f(ox)} G°_{CuAl_2O_4} / (\text{kJ mol}^{-1}) \pm 0.957 = -18.40 + 0.00816T/K. \quad (1074 - 1232\ K) \qquad (47)$$

The comparison of copper aluminates stability functions given in Equations (46) and (47) with the results obtained in the previous studies by various methods is provided in Tables 7 and 8.

Table 7. $\Delta_{f(ox)} G°_{CuAlO_2}$ determined in the present work and compared with the results of the previous studies.

$\Delta_{f(ox)} G°_{CuAlO_2}$ / (kJ mol^{-1})	T / K	Experimental method	Reference
− 8.37	1273	EMF	[33]
− 19.66 + 0.00879T/K	*	TGA at various P_{O_2}	[71]
− 55.65 + 0.04167T/K	973-1273	H_2/H_2O equilibria	[72]
14.52 − 0.01998T/K	1073-1273	EMF	[69]

– 11.86 + 0.00521T/K	973-1323	EMF	[68]
– 43.78 + 0.03054T/K	1051-1265	EMF	This study

*calculated by an extrapolation of two equilibria, one was measured from 1300 to 1350 K, the other one from 1450 to 1490 K.

Table 8. $\Delta_{f(ox)}G^{\circ}_{CuAl_2O_4}$ determined in the present work and compared with the results of the previous studies.

$\Delta_{f(ox)}G^{\circ}_{CuAl_2O_4}$ / (kJ mol^{-1})	T / K	Experimental method	Reference
– 30.12 + 0.01004T/K	*	TGA at various P_{O_2}	[71]
18.42 – 0.02079T/K	973-1323	EMF	[68]
30.71 – 0.04477T/K	1073-1273	EMF	[69]
– 18.40 + 0.00816T/K	1074-1232	EMF	This study

*calculated by an extrapolation of two equilibria, one was measured from 1300 to 1350 K, the other one from 1450 to 1490 K.

Table 7 shows a certain scatter among the reported $\Delta_{f(ox)}G^{\circ}_{CuAlO_2}$ data, however they fairly agree except the results reported by Slobodyanyuk et al. [69]. Contrary, the standard Gibbs energy of formation of $CuAl_2O_4$ from its component oxides shows a high scatter among the reports summarized in Table 8. It can be explained by the fact that in the electrochemical studies [68 and 69] (including the present work) the $\Delta_{f(ox)}G^{\circ}_{CuAl_2O_4}$ was calculated from several individual reaction equilibria and measured with several individual galvanic cells, therefore possible experimental errors were accumulated and resulted in this discrepancy (Table 8). Particularly, the slope reported by [68] is opposite to the slope reported in this study. Therefore, the decomposition temperature of $CuAl_2O_4$ into its component oxides reported as 885 K derived from [68] by extrapolation of $\Delta_{f(ox)}G^{\circ}_{CuAl_2O_4}$ to low temperatures requires a reconsideration. Even though, Navrotsky and Kleppa [74] measured calorimetrically the standard enthalpy of formation of $CuAl_2O_4$ from its component oxides as 21.63±0.79 kJ mol^{-1}

5 Conclusions

The EMF method with solid state electrolyte is a powerful experimental tool providing accurate thermodynamic data of solutions and substances, which are necessary for modelling equilibria of chemical reactions and the phase stabilities. The purpose of the present work was an attempt to increase knowledge concerning thermodynamic stabilities of selected phases in the MgO-Sb-O, CaO-Te-O, Pt-Te-O, and Al_2O_3-Cu-O systems at various temperatures.

Particularly, thermodynamic properties of $MgSb_2O_4$, Ca_3TeO_6, PtTe, Cu_2O, CuO, $CuAlO_2$, and $CuAl_2O_4$ were determined by the EMF method with oxygen concentration galvanic cells based on solid oxide electrolytes.

New sets of thermodynamic data were provided for $MgSb_2O_4$, Cu_2O, CuO, $CuAlO_2$, and $CuAl_2O_4$ and an attempt to reveal existing discrepancies among the previous studies was done. High temperature thermodynamic properties of Ca_3TeO_6 and PtTe were determined for the first time.

Particular attention was paid to the accuracy and precision of temperature and EMF measurements, applying the state-of-the-art equipment.

The thermodynamic data reported in the present work should be of a great interest for extractive metallurgy to design, improve, and troubleshoot diverse industrial processes. Moreover, they can be utilized in a development of composite and functional materials and product developing work.

6 References

1. "Critical raw materials for the EU" Report of the Ad hoc Working Group on defining critical raw materials, 30 July 2010.
2. "Report on the critical raw materials for the EU" Report of the Ad hoc Working Group on defining critical raw materials, May 2014.
3. Extractive Metallurgy of Copper (Chapter 18), M.E. Schlesinger, M.J. King, K.C. Sole, W.G.I. Davenport (2011) 5th ed., Elsevier, Oxford.
4. MTDATA and the Prediction of Phase Equilibria in Oxide Systems: 30 Years of Industrial Collaboration, Metallurgical and Materials Transactions B: Process Metallurgy and Materials Processing Science (2016) ahead of print.
5. Z. Moser, K. Fitzner, The use of experimental thermodynamic data in the phase equilibria verification, Thermochimica Acta 332 (1999) 1-19.
6. Fundamentals of metallurgical processes, L. Coudurier, D.W. Hopkins, I. Wilkomirsky (1985) 2nd edition, Pergamon Press, Oxford.
7. I. Katayama, S. Sygimura, Z. Kozuka, Measurements of standard molar Gibbs energies of formation of Sb_2O_3, $ZnSb_2O_4$ and $MgSb_2O_4$ by the emf method with zirconia solid electrolyte, Transactions of the Japan Institute of Metals 28 (1987) 406-411.
8. N. Kemori, W. Denholm, S. Saunders, Measurements of standard Gibbs energies of formation pf Sb_2O_3, $MgSb_2O_4$ and $Ca_4Sb_2O_7$ by an EMF method, Canadian Metallurgical Quarterly 35 (1996) 269-274.
9. S. Raghavan, Gibbs energy of formation of magnesium antimonite ($MgSb_2O_4$) using a magnesium fluoride solid electrolyte galvanic cell, Transactions of the Indian Institute of Metals 51(6) (1998) 511-513.
10. S.A. Malyutin, K.K. Samplavskaya, M.Kh. Karapet'yants, Thermographic study of a calcium oxide-tellurium dioxide system, Trudy Instituta – Moskovskii Khimiko-Tekhnologicheskii Institut imeni D. I. Mendeleeva 62 (1969) 50-52.
11. R. Mishra, P.N. Namboodiri, S.N. Tripathi, S.R. Dharwadkar, Partial phase diagram of CaO-TeO_2 system, Journal of Alloys and Compounds 280(1-2) (1998) 56-64.
12. R. Mishra, S.R. Bharadwaj, A.S. Kerkar, S.R. Dharwadkar, Determination of the Gibb's energy of formation of $CaTeO_3$ and $CaTe_2O_5$ by the transpiration technique, Journal of Alloys and Compounds 248 (1997) 80-85.
13. S.N. Tripathi, R. Mishra, M.D. Mathews, P.N. Namboodiri, X-ray powder diffraction investigation of new high temperature polymorphs of $CaTeO_3$ and $CaTe_2O_5$, Powder Diffraction 16(4) (2001) 205-211.
14. B. Stöger, M. Weil, E. Zobetz, G. Giester, Polymorphism of $CaTeO_3$ and solid solutions $Ca_xSr_{1-x}TeO_3$, Acta Crystallographica B65 (2009) 167–181.
15. T.A. Stolyarova, E.G. Osadchii, Standard Thermodynamic Properties of Pd and Pt Ditellurides, Geochemistry International 49(10) (2011) 1043-1047.

16. T.A. Stolyarova, E.G. Osadchii, Enthalpy of Formation pf Platinum and Palladium Monotellurides from the Elements, Geochemistry International 51(10) (2013) 852-854.
17. M.L. Gimpl, C.E. Nelson, N. Fuschillo, The Pt-Te system, ASM Transactions Quarterly 56 (1963) 209-213.
18. S. Bhan, T. Goedecke, K. Schubert, Phase diagrams of systems of platinum with tin, antimony, and tellurium, Journal of the Less-Common Metals 19(2) (1969) 121-140.
19. S.G. Rybkin, A.A. Krapivko, Platinum- tellurium system in the range 28-66.7 at.% tellurium, Neorganicheskie Materialy 28(7) (1992) 1534-1536.
20. W.-S. Kim, Re-investigation of the phase constitution of the system Pt-Te, Metals and Materials (Seoul) 2(1) (1996) 9-14.
21. C. Guo, L. Huang, C. Li, S. Shang, Z. Du, Thermodynamic Modelling of the Pt-Te and Pt-Sb-Te Systems, Journal of Electronic Materials 44(8) (2015) 2638-2650.
22. F. Grønvold, T. Thurmann-Moe, E.F. Westrum Jr., E. Chang, Low-Temperature Heat Capacities and Thermodynamic Functions of Some Platinum and Palladium Group Chalcogenides. I. Monochalcogenides; PtS, PtTe, and PdTe, the Journal of Chemical Physics 35 (1961) 1665-1669.
23. E.F. Westrum Jr., H.G. Carlson, F. Grønvold, A. Kjekshus, Low-Temperature Heat Capacities and Thermodynamic Functions of Some Palladium and Platinum Group Chalcogenides. II. Dichalcogenides; PtS_2, $PtTe_2$, and $PdTe_2$, the Journal of Chemical Physics 35 (1961) 1670-1676.
24. V.K. Karzhavin, Sulfides, Selenides, and Tellurides of Platinum and Palladium: Estimation of Thermodynamic Properties, Geochemistry International 45(9) (2007) 931-937.
25. T. Fujimura, S.-I. Tanaka, In-situ high temperature X-ray diffraction study of Cu/Al_2O_3 interface reactions, Acta Materialia 46(9) (1998) 3057-3061.
26. C.W. Seager, K. Kokini, K. Trumble, M.J.M. Krane, The influence of $CuAlO_2$ on the strength of eutectically bonded Cu/Al_2O_3 interfaces, Scripta Materialia 46 (2002) 395-400.
27. M. Arjmand, C.S. Knee, H. Leion, T. Mattisson, Standard enthalpy of formation of $CuAl_2O_4$ revisited, Chemical Engineering Communications 202(5) (2015) 694-697.
28. D. Shishin, S.A. Decterov, Critical assessment and thermodynamic modeling of the Cu-O and Cu-O-S systems, CALPHAD 38 (2012) 59-70.
29. H.S. Roberts, F.H. Smith, The system copper: cupric oxide: oxygen, Journal of the American Ceramic Society 43 (1921) 1061-1070.
30. K. Fitzner, Z. Moser, Activity of oxygen in dilute liquid copper-oxygen alloys, Metals Technology (London) 6(7) (1979) 273-275.
31. A. Boudene, K. Hack, A. Mohammad, D. Neuschutz, E. Zimmermann, Experimental investigation and thermochemical assessment of the system copper-oxygen, Zeitschrift fuer Metallkunde 83(9) (1992) 663-668.
32. A.V. Kosenko, G.A. Emel'chenko, Equilibrium Phase Relationships in the System Cu-O under High Oxygen Pressure, Journal of Phase Equilibria 22(1) (2001) 12-19.
33. H. Schmalzried, Measurement of the free enthalpy of reaction in the formation of spinel phases from the single oxides by aid of solid galvanic couples, Zeitschrift fuer Physikalische Chemie (Muenchen, Germany) 25 (1960) 178-192.

34. S.K. Misra, A.C.D. Chaklader, The system copper oxide – alumina, Journal of the American Ceramic Society 46(10) (1963) 509.
35. T. Tsuchida, R. Furuichi, T. Sukegawa, M. Furudate, T. Ishii, Thermoanalytical study on the reaction of the CuO-Al_2O_3 (η, γ and α) systems, Thermochimica Acta 78(1-3) (1984) 71-80.
36. M. Guedes, J.M.F. Ferreira, A.C. Ferro, A study on CuO-Al_2O_3 reaction paths, Advances in Powder Metallurgy and Particulate Materials (2008) 5/1-5/13.
37. M. Chen, B. Zhao, Phase Equilibrium Studies of Cu_2O-SiO_2-Al_2O_3 System in Equilibrium with Metallic Copper, Journal of the American Ceramic Society 96(11) (2013) 3631-3636.
38. N. Hellstén, J. Hamuyuni, P. Taskinen, High-temperature phase equilibria of Cu-O-Al_2O_3 system in air, Canadian Metallurgical Quarterly 55(2) (2016) 226-233.
39. The CRC Handbook of Solid State Electrochemistry, Edited by P.J. Gellings, H.J.M. Bouwmeester (1997) CRC Press.
40. Solid Electrolytes and Their Applications, Edited by E.C. Subbarao (1980) Plenum Press, New York.
41. K. Kiukkola, C. Wagner, Galvanic cells for the determination of the standard molar free energy of formation of metal halides, oxides, and sulfides at elevated temperatures, Journal of Electrochemical Society 104 (1957) 308-316.
42. J.B. Wagner, C. Wagner, Determination of the standard free energy of formation of cuprous sulfide at 300°, Journal of Electrochemical Society 104 (1957) 509-511.
43. Treatise on Solid State Chemistry, vol. 4 “Reactivity of Solids”, Edited by N.B. Hannay (1976) Plenum Press, New York.
44. S.P.S. Badwal, Zirconia-based solid electrolytes: microstructure, stability and ionic conductivity, Solid State Ionics 52(1-3) (1992) 23-32.
45. Handbook of solid state electrochemistry, vol. 1 “Fundamentals, Methodologies, Applications”, Edited by V.V. Kharton (2009) Wiley-VCH, Weinheim.
46. J.N. Pratt, Applications of Solid Electrolytes in Thermodynamic Studies of Materials: A Review, Metallurgical Transactions 21A (1990) 1223-1250.
47. P. Duwez, F. Odell, F.H.Jr. Brown, Stabilization of Zirconia with Calcia and Magnesia, Journal of the American Ceramic Society 35 (1952) 107-113.
48. MTOX Database, version 8.2, NPL, Teddington, UK.
49. H. Schmalzried, Zirconium dioxide as an electrolyte for electrochemical studies at high temperatures, Zeitschrift fuer Elektrochemie und Angewandte Physikalische Chemie 66 (1962) 572-576.
50. B.C.H. Steele, C.B. Alcock, Factors influencing the performance of solid oxide electrolytes in high-temperature thermodynamic measurements, Transactions of the American Institute of Mining, Metallurgical and Petroleum Engineers 233(7) (1965) 1359-1367.
51. V.V. Kharton, F.M.B. Marques, A. Atkinson, Transport properties of solid oxide electrolyte ceramics: a brief review, Solid State Ionics 174 (2004) 135 – 149.
52. H. Ipser, A. Mikula, I. Katayama, Overview: the emf method as a source of experimental thermodynamic data, CALPHAD 34 (2010) 271–278.
53. H. Taimatsu, K. Miyatake, H. Kaneko, F. Nakatani, Reactions between stabilized zirconia for oxygen sensor and iron oxides, Nippon Kinzoku Gakkaishi 46(5) (1982) 480-486.

54. B. Heshmatpour, D.A. Stevenson, Experimental problems in the use of solid oxide electrolytes, Journal of Applied Electrochemistry 11(4) (1981) 433-442.
55. IUPAC Physical and Biophysical Chemistry Division. Quantities, Units, and Symbols in Physical Chemistry, 3rd ed. (The Green Book). Prepared for publication by E.R. Cohen, T. Cvitaš, J.G. Frey, B. Holmström, K. Kuchitsu, R. Marquardt, I. Mills, F. Pavese, M. Quack, J. Stohner, H.L. Strauss, M. Takami, A.J. Thor (2007) The Royal Society of Chemistry: Cambridge, U.K.
56. M. Aspiala, D. Sukhomlinov, P. Taskinen, Standard Gibbs energy of formation of tellurium dioxide measurement by a solid-oxide electrolyte EMF technique, Thermochimica Acta 573 (2013) 95–100.
57. M. Aspiala, D. Sukhomlinov, P. Taskinen, Standard thermodynamic properties of Bi_2O_3 by a solid-oxide electrolyte EMF technique, Journal of Chemical Thermodynamics 75 (2014) 8–12.
58. M. Aspiala, D. Sukhomlinov, P. Taskinen, Determination of Standard Thermodynamic Properties of Sb_2O_3 by a Solid-Oxide Electrolyte EMF Technique, Solid State Ionics 265 (2014) 80–84.
59. H. Ono, M. Nakahata, F. Tsukihashi, N. Sano, Determination of standard Gibbs energies of formation of MgO, SrO, and BaO, Metallurgical and Materials Transactions B 24(3) (1993) 487-492.
60. Scientific Group Thermodata Europe (SGTE) database. Available: http://www.sgte.org.
61. M. Sahu, D. Rawat, B.G. Vats, M.K. Saxena, S. Dash, Thermo physico-chemical investigations on A-Te-O (A = Cr, Fe, Ni) system, Thermochimica Acta 585 (2014) 50-62.
62. J. Leitner, P. Vonka, D. Sedmidubsky, P. Svoboda, Application of Neumann-Kopp rule for the estimation of heat capacity of mixed oxides, Thermochimica Acta 497 (2010) 7-13.
63. Thermochemical properties of inorganic substances, I. Barin, O. Knacke (1973) Springer-Verlag, Berlin/Heidelberg/New York, Verlag Stahleisen mbH Düsseldorf.
64. Thermochemical Data of Pure Substances, part II, I. Barin (1989) VCH Verlagsgesellschaft, Weinheim/VCH Publishers, New York.
65. W.A. Dutton, W.C. Cooper, the Oxides and Oxyacids of Tellurium, Chemical Reviews 66 (1966) 657–675.
66. J.R. Soulen, P. Sthapitanonda, J.L. Margrave, Vaporization of Inorganic Substances: B_2O_3, TeO_2 and Mg_3N_2, the Journal of Physical Chemistry 59 (1955) 132–136.
67. MTDATA-phase diagram software from the National Physical Laboratory (NPL), SGTE pure element transition data. Available: http://mtdata.software.googlepages.com/unarytable.html.
68. K.T. Jacob, C.B. Alcock, Thermodynamics of $CuAlO_2$ and $CuAl_2O_4$ and Phase Equilibria in the System Cu_2O-CuO-Al_2O_3, Journal of the American Ceramic Society 58(5-6) (1975) 192-195.
69. A.A. Slobodyanyuk, Yu.D. Tret'yakov, A.F. Bessonov, Thermodynamic stability of copper silicates and aluminates studied by emf. with a solid electrolyte, Zhurnal Fizicheskoi Khimii 45(7) (1971) 1871-1872.
70. R.D. Holmes, H.S.C. O'Neill, R.J. Arculus, Standard Gibbs free energy of formation for Cu_2O, NiO, CoO, and Fe_xO: High resolution electrochemical measurements using zirconia solid electrolytes from 900-1400 K, Geochimica et Cosmochimica Acta 50(11) (1986) 2439-2452.

71. A.M.M. Gadalla, J. White, Equilibrium relation in the system Cu_2O-CuO-Al_2O_3, British Ceramic Transactions and Journal 63(1) (1964) 39-62.
72. A.G. Zalazinskii, V.F. Balakirev, N.M. Chebotaev, G.I. Chufarov, Thermodynamic analysis of the reduction, dissociation, and formation of copper aluminate, copper chromate(III), and copper ferrate(II) from the free elements and oxides, Zhurnal Neorganicheskoi Khimii 14(3) (1969) 624-626.
73. Thermochemical Data of Pure Substances, part I, I. Barin (1989) VCH Verlagsgesellschaft, Weinheim/VCH Publishers, New York.
74. A. Navrotsky, O.J. Kleppa, Thermodynamics of formation of simple spinels, Journal of Inorg Nucl Chem 30(2) (1968) 479-498.

Aalto-DD 5/2017

ISBN 978-952-60-7243-2 (printed)
ISBN 978-952-60-7242-5 (pdf)
ISSN-L 1799-4934
ISSN 1799-4934 (printed)
ISSN 1799-4942 (pdf)

Aalto University
School of Chemical Technology
Department of Materials Science and Engineering
www.aalto.fi

BUSINESS +
ECONOMY

ART +
DESIGN +
ARCHITECTURE

SCIENCE +
TECHNOLOGY

CROSSOVER

**DOCTORAL
DISSERTATIONS**